



**HAL**  
open science

## Z-Scheme g-C<sub>3</sub>N<sub>4</sub>/Fe<sub>3</sub>O<sub>4</sub>/Ag<sub>3</sub>PO<sub>4</sub> @Sep magnetic nanocomposites as heterojunction photocatalysts for green malachite degradation and dynamic molecular studies

R. Haounati, H. Ighnih, H. Ouachtak, Rahime Eshaghi Malekshah, N. Hafid, A. Jada, A. Ait Addi

### ► To cite this version:

R. Haounati, H. Ighnih, H. Ouachtak, Rahime Eshaghi Malekshah, N. Hafid, et al.. Z-Scheme g-C<sub>3</sub>N<sub>4</sub>/Fe<sub>3</sub>O<sub>4</sub>/Ag<sub>3</sub>PO<sub>4</sub> @Sep magnetic nanocomposites as heterojunction photocatalysts for green malachite degradation and dynamic molecular studies. *Colloids and Surfaces A: Physicochemical and Engineering Aspects*, 2023, 671, pp.131509. 10.1016/j.colsurfa.2023.131509 . hal-04297898

**HAL Id: hal-04297898**

**<https://hal.science/hal-04297898v1>**

Submitted on 22 Nov 2023

**HAL** is a multi-disciplinary open access archive for the deposit and dissemination of scientific research documents, whether they are published or not. The documents may come from teaching and research institutions in France or abroad, or from public or private research centers.

L'archive ouverte pluridisciplinaire **HAL**, est destinée au dépôt et à la diffusion de documents scientifiques de niveau recherche, publiés ou non, émanant des établissements d'enseignement et de recherche français ou étrangers, des laboratoires publics ou privés.

1           **Z-Scheme g-C<sub>3</sub>N<sub>4</sub>/Fe<sub>3</sub>O<sub>4</sub>/Ag<sub>3</sub>PO<sub>4</sub>@Sep magnetic nanocomposites as**  
2           **heterojunction photocatalysts for green malachite degradation and**  
3           **Dynamic molecular studies**

4 R. Haounati <sup>1, \*</sup>, H. Ighnih <sup>1</sup>, H. Ouachtak <sup>1,2,\*</sup>, Rahime Eshaghi Malekshah <sup>3</sup>, N. Hafid <sup>4</sup>, A.  
5 Jada <sup>5,6,\*</sup>, A. Ait addi <sup>1</sup>

6 <sup>1</sup> Physical Chemistry & Environment Team, Faculty of Sciences, Ibn Zohr University,  
7 Agadir, Morocco.

8 <sup>2</sup> Department of Applied Chemistry, Faculty of Applied Sciences, Ibn Zohr University,  
9 Ait Melloul, Morocco.

10 <sup>3</sup>Medical Biomaterial Research Centre (MBRC), Tehran University of Medical Sciences,  
11 Tehran, Iran

12 <sup>4</sup> Center For Education & Training Profession Souss Massa, Morocco.

13 <sup>5</sup> Institute of Materials Science of Mulhouse (IS2M), Haute Alsace University, Mulhouse  
14 68100, France.

15 <sup>6</sup> Strasbourg University, Strasbourg 67081, France.

16 \*Corresponding authors:

17 amane.jada@uha.fr ; ouachtakhassan@gmail.com ; haounati.redouane@gmail.com

18

19

20

21

22

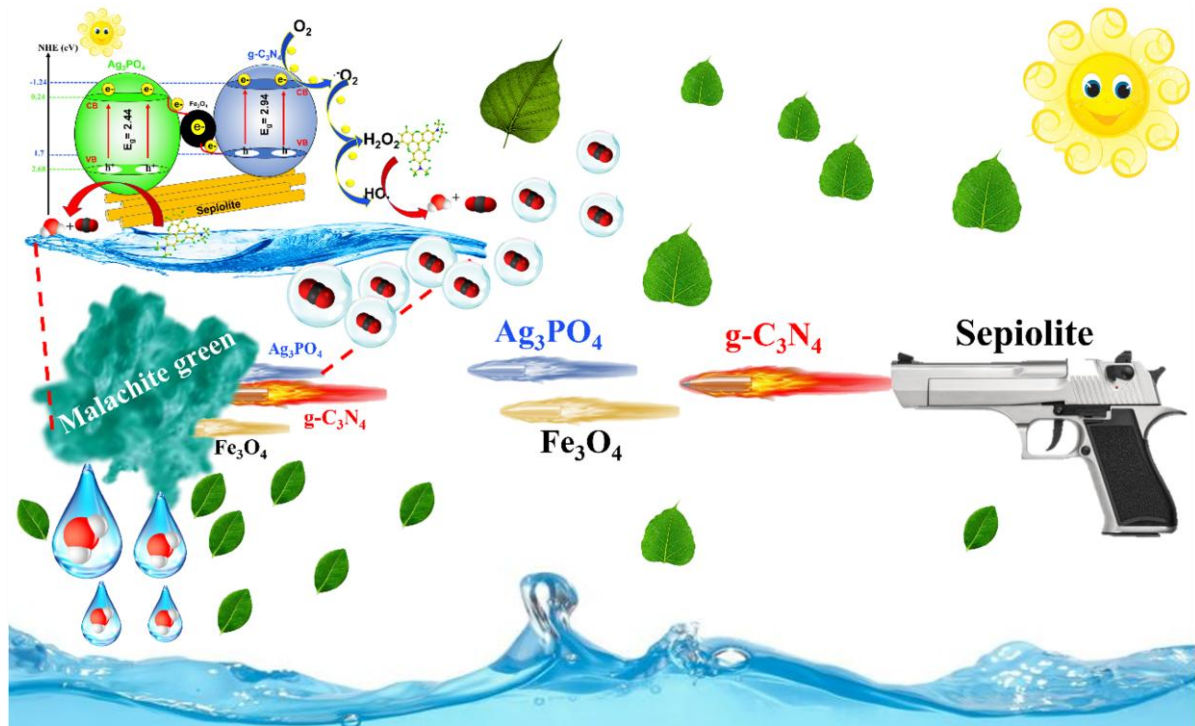
23

24

25

26

27 **Graphical abstract**



28

29 **Abstract**

30 Recently, the synthesis of Z-scheme nanocomposite heterojunctions has received significant  
31 attention. In the present work, we prepared a Z-scheme heterostructures nanocomposite by  
32 using a facile co-precipitation method. Several techniques were used to characterize the  
33 structures, the morphologies, the optical and the electronic properties, as well as the  
34 photocatalytic performance of the nanocomposite. Thus, the scanning electron microscope  
35 and the transmission electron microscope analyses showed that the sepiolite surface was well  
36 occupied by the  $\text{Ag}_3\text{PO}_4$ , the  $\text{g-C}_3\text{N}_4$  and the  $\text{Fe}_3\text{O}_4$  nanoparticles. Further, the  $\text{g-}$   
37  $\text{C}_3\text{N}_4/\text{Fe}_3\text{O}_4/\text{Ag}_3\text{PO}_4@\text{Sep}$  nanocomposite, as compared to pure  $\text{g-C}_3\text{N}_4$ ,  $\text{g-C}_3\text{N}_4@\text{Sep}$  and  $\text{g-}$   
38  $\text{C}_3\text{N}_4/\text{Ag}_3\text{PO}_4@\text{Sep}$ , exhibited significantly improved photocatalytic performance for the  
39 degradation of malachite green (MG) (100%, 12 min). Such photocatalytic activity was found  
40 to be about 27, 26 and 1.85 times higher than that of  $\text{g-C}_3\text{N}_4$ ,  $\text{g-C}_3\text{N}_4@\text{Sep}$  and  $\text{g-}$   
41  $\text{C}_3\text{N}_4/\text{Ag}_3\text{PO}_4@\text{Sep}$ , respectively. The photocatalytic enhancement of magnetic  
42 nanocomposite  $\text{g-C}_3\text{N}_4/\text{Fe}_3\text{O}_4/\text{Ag}_3\text{PO}_4@\text{Sep}$  to degrade organic molecules such as MG dye,  
43 under solar light irradiation, was attributed to the synergy effects between  $\text{Ag}_3\text{PO}_4$  supported  
44 by sepiolite clay and  $\text{g-C}_3\text{N}_4$  combined with the  $\text{Fe}_3\text{O}_4$  nanoparticles. Furthermore, the

45 photocatalytic activity of g-C<sub>3</sub>N<sub>4</sub>/Fe<sub>3</sub>O<sub>4</sub>/Ag<sub>3</sub>PO<sub>4</sub>@Sep remained at a high level even after four  
46 cycles, suggesting that the quaternary nanocomposite has a high stability and good reusability,  
47 as resulting from the suitable band structure and the Z-scheme heterojunction construction,  
48 which improved the light usage and the charge carrier migration rate. DFT-D correction was  
49 used to optimize all the structures. Then, MD calculations were applied to form  
50 Fe<sub>3</sub>O<sub>4</sub>/Ag<sub>3</sub>PO<sub>4</sub>@Sep nano-composite, resulting the stable configuration due to the negative  
51 adsorption. At last, the MG adsorption was investigated by adsorption locator module on  
52 nano-composite, suggesting the thermodynamic stability system.

53 **Keywords:** Z-scheme, nanocomposite, malachite green, MD calculation.

54

55

56

57

58

59

60

61

62

63

64

65

66

67

68

## 70 **1. Introduction**

71 In the recent years, the aquatic systems pollution has led to several humans and animals health  
72 issues, impacting the economy and affecting the climate change [1–4]. Such water pollution  
73 results mainly from the growing industrialization and the agricultural activities, and leads to  
74 wastewater large amounts production [5]. The polluted waters may contain toxic metals,  
75 organic molecules, dyes and drugs [6]. Particularly, the dye effluents originating from textile,  
76 leather, cosmetics and pigments industries, are responsible for one of the major water  
77 pollution problems in the world, and they should be consequently investigated [7].

78 Several methods such as the physical adsorption [8, 9], the biological process [10], and the  
79 chemical oxidation [11, 12], have been applied at laboratory, as well as, at large scales, for the  
80 wastewater treatment and the dye removal from the contaminated aqueous medium. Among  
81 these methods, the Advanced Oxidation Processes (AOP), such as: photocatalytic degradation  
82 using heterogeneous photocatalytic process, has been found to be a superior method, due to its  
83 operational simplicity, its high efficiency toward the organic dyes, its economic benefits and  
84 its facile mineralization of organic dyes into  $H_2O$  and  $CO_2$  [13]. On the other hand, various  
85 materials used as adsorbents and/or catalysts, for the dye removal from wastewaters using the  
86 AOP method, they mainly include few high surface area materials such as zeolite, activated  
87 carbon, carbon nanotubes, graphene and some other photocatalytic materials such as oxides  
88 ( $ZnO$ ,  $Bi_2O_3$ ,  $TiO_2$ ,  $YVO_4$ ,  $WO_3$ ), hydroxides ( $La(OH)_3$ ), sulfurs ( $MoS_2$ ) and phosphates  
89 ( $BiPO_4$ ,  $CePO_4$ ,  $Ag_3PO_4$ ) [13, 14]. For the silver orthophosphate ( $Ag_3PO_4$ ) based  
90 semiconductor photocatalysts, due to their strong oxidation abilities, and their non-toxicities,  
91 they have been widely employed for water purification [15]. In addition, to enhance the  
92 catalytic activity of these silver orthophosphate ( $Ag_3PO_4$ ) based materials, several  
93 modifications were realized, including: homojunction construction, Z-Scheme composite  
94 design, and defect generation [16]. The Z-Scheme design consist on improving the separation  
95 efficiency of photogenerated electron(-)-hole(+) pairs by constructing heterojunction Z-  
96 scheme photocatalysts with typical n-type semiconductors, such as:  $CeO_2$ ,  $TiO_2$ ,  $Fe_2O_3$ ,  $ZnO$ ,  
97 etc.[13]. There are many problems associated with Z-scheme photocatalysts materials,  
98 including the problem of charge transport at incomplete contact interfaces [17], and the  
99 sufferance from the recycling process [13].

100 The present work deals with novel “g-C<sub>3</sub>N<sub>4</sub> /Fe<sub>3</sub>O<sub>4</sub> /Ag<sub>3</sub>PO<sub>4</sub>@Sep” Z-scheme based  
101 photocatalysts, which were prepared, using a simple co-precipitation approach, to enhance the  
102 sunlight degradation of Malachite Green MG dye in water. To the best of our knowledge,  
103 there are no reported work on the preparation and the application of this material in the  
104 photocatalytic decomposition performance of dyes under sunlight irradiation.

105 In the Z-scheme based photocatalyst preparation, the Fe<sub>3</sub>O<sub>4</sub> was used as an n-type  
106 semiconductor, due to its strong magnetic properties, the sepiolite clay (having the chemical  
107 formula: Mg<sub>4</sub>Si<sub>6</sub>O<sub>15</sub>(OH)<sub>2</sub>·6H<sub>2</sub>O) was used for its important benefits (environmentally  
108 friendly, stable, inexpensive), and its large specific surface area, the g-C<sub>3</sub>N<sub>4</sub> was used since it  
109 is considered as a major component in the design of new photocatalysts for photodegradation  
110 of organic molecules such as dyes under sunlight irradiation. The high photocatalytic activity  
111 of the g-C<sub>3</sub>N<sub>4</sub> can be explained by its band gap of 2.7 eV, yielding to an absorption edge  
112 suitable for visible light capture, and band positions suitable for water oxidation-reduction,  
113 and leading to high thermal and chemical stabilities[18, 19].It should be noted that the  
114 sepiolite can provide more active sites for the Z-scheme “g-C<sub>3</sub>N<sub>4</sub>/Fe<sub>3</sub>O<sub>4</sub>/Ag<sub>3</sub>PO<sub>4</sub>”  
115 photocatalyst.

116 In the present work, the structure and the morphology of the elaborated photocatalysts were  
117 investigated. Further, we propose a possible enhanced Z-scheme heterojunction mechanism of  
118 electron transfer. MD simulation was used to form Fe<sub>3</sub>O<sub>4</sub>/Ag<sub>3</sub>PO<sub>4</sub>@Sep nano-composite and  
119 MG adsorption on this nano-composite.

## 120 **2. Experimental**

### 121 **2.1. Samples preparation**

#### 122 **2.1.1. Chemicals**

123 The raw clay used in this work is sepiolite (Sep), is the same as used elsewhere [20].The other  
124 chemicals, including melamine (C<sub>3</sub>H<sub>6</sub>N<sub>6</sub>, 99%), ferric chloride hexahydrate (FeCl<sub>3</sub>·6H<sub>2</sub>O,  
125 97%), ferrous sulfate hepta hydrate (FeSO<sub>4</sub>·7H<sub>2</sub>O, 99%), silver nitrate (AgNO<sub>3</sub>, 99.8%),  
126 ammonium dihydrogen phosphate (NH<sub>4</sub>H<sub>2</sub>PO<sub>4</sub>, 98%),hydrochloric acid (HCl, 99%), sodium  
127 hydroxide (NaOH, 98%), malachite green (MG, 99%) and ethylene glycol (HOCH<sub>2</sub>CH<sub>2</sub>OH,  
128 99%), were all of analytical grade, purchased from Sigma-Aldrich and used as received.

129

#### 130 **2.1.2 Synthesis of g-C<sub>3</sub>N<sub>4</sub> and Fe<sub>3</sub>O<sub>4</sub>**

131 The g-C<sub>3</sub>N<sub>4</sub> photocatalyst was synthesized through simple melamine calcination, by heating,  
132 at 550 °C for 3 h (heating rate of 5 °C/min) 5g of melamine powder, and by using an alumina  
133 crucible placed in a muffle furnace, as depicted in **Figure.1**.

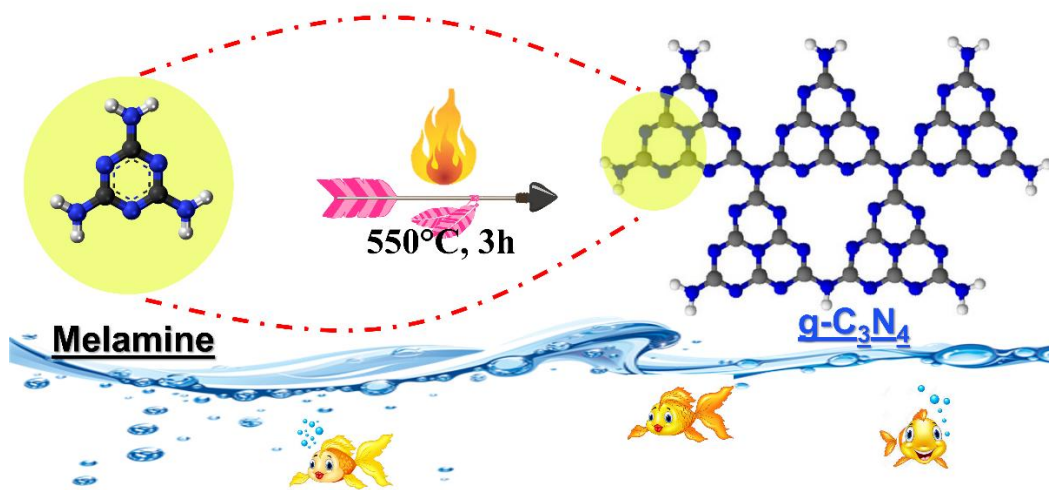


**Figure. 1:** Mechanism of g-C<sub>3</sub>N<sub>4</sub> preparation from melamine

134  
135 The magnetite Fe<sub>3</sub>O<sub>4</sub> was prepared by co-precipitation method. Thus, in typical experiment,  
136 4.670 g of FeCl<sub>3</sub>.6H<sub>2</sub>O and 2.401 g of FeSO<sub>4</sub>.7H<sub>2</sub>O were dissolved in 50 ml of ethylene  
137 glycol/deionized water with the ratio 1/1 under vigorous magnetic stirrer at room temperature  
138 for 30 min under N<sub>2</sub>. Then amounts of NaOH 1M solution were added dropwise to the  
139 previous solution, under constant magnetic stirring to adjust the pH to 9. Afterwards, the  
140 mixture was magnetically stirred for 12 h more. Subsequently, the obtained mixture was  
141 washed with distilled water, and the resulting black Fe<sub>3</sub>O<sub>4</sub> was dried at 80 °C for 24 h as  
142 shown in **Figure.2**.

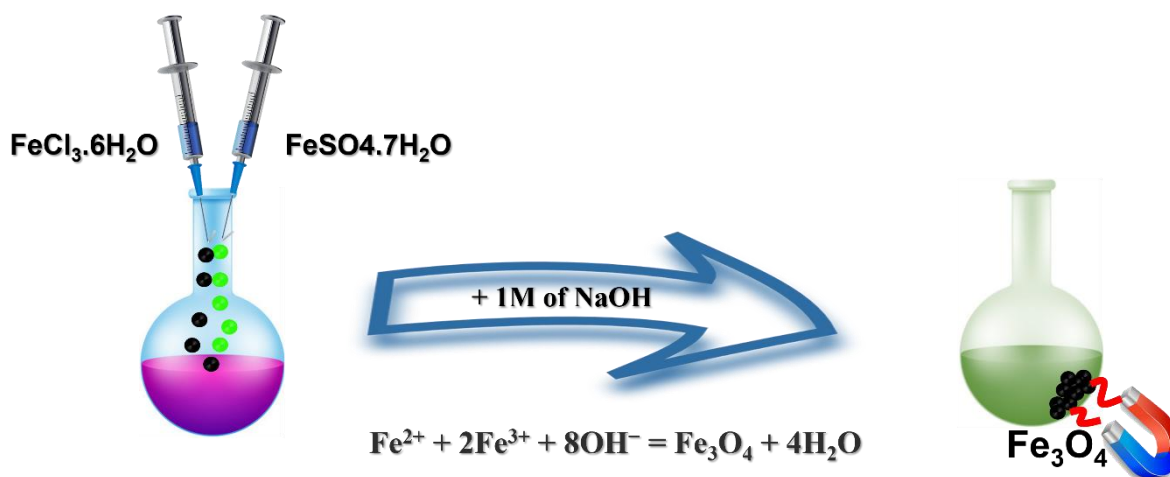


**Figure. 2:** The scheme for the  $\text{Fe}_3\text{O}_4$  nanoparticles formation

143

### 144 2.1.3 Synthesis of quaternary $\text{g-C}_3\text{N}_4/\text{Fe}_3\text{O}_4/\text{Ag}_3\text{PO}_4@\text{Sep}$ nanocomposites

145 The  $\text{g-C}_3\text{N}_4/\text{Fe}_3\text{O}_4/\text{Ag}_3\text{PO}_4@\text{Sep}$  nanocomposite was prepared by a facile heterogeneous  
 146 suspension reaction procedure.

147 Firstly, the sepiolite-supported- $\text{Ag}_3\text{PO}_4$  ( $\text{Ag}_3\text{PO}_4@\text{Sep}$ ) nanocomposite was synthesized  
 148 through a simple electrostatically driven reaction. Thus, in a typical experimental synthesis  
 149 procedure, a sepiolite suspension was obtained by dispersing 4 g of the raw sepiolite in  
 150 200 mL of distilled water using ultrasonic treatment. Afterwards, a solution of  $\text{AgNO}_3$  was  
 151 added dropwise to the aqueous sepiolite dispersion in order to recover totally the negatively  
 152 charged sepiolite sheets by the positive  $\text{Ag}^+$  charges. Subsequently, 0.048 mM  $\text{NH}_4\text{H}_2\text{PO}_4$   
 153 was added, drop by drop, to the sepiolite- $\text{AgNO}_3$  mixture and  $\text{NaOH}$  0.5M was slowly added  
 154 into the resulting mixture, followed by magnetic stirring at room temperature for 4 h. At the  
 155 end of the reaction, a green-yellow precipitate of  $\text{Ag}_3\text{PO}_4@\text{Sep}$  was recovered by  
 156 centrifugation at 5000 rpm for 10 min, washed several times with distilled water, and dried at  
 157 80 °C overnight.

158 Secondly, the magnetic nanocomposite ( $\text{Fe}_3\text{O}_4/\text{Ag}_3\text{PO}_4@\text{Sep}$ ) was prepared by dropping off  
 159  $\text{Fe}_3\text{O}_4$  nanoparticles (10 mg/mL) on the surface of the heterogeneous  $\text{Ag}_3\text{PO}_4@\text{Sep}$   
 160 suspension, under vigorous stirring for 4 h. The resulting magnetic nanocomposite  
 161  $\text{Fe}_3\text{O}_4/\text{Ag}_3\text{PO}_4@\text{Sep}$  was collected by a permanent magnet, washed with distilled water  
 162 multiple times, and dried under vacuum overnight. In the last step, a  $\text{g-C}_3\text{N}_4$  suspension was  
 163 dropped off the surface of the  $\text{Fe}_3\text{O}_4/\text{Ag}_3\text{PO}_4@\text{Sep}$  nanocomposite. Finally, the obtained  
 164 magnetic nanocomposite was separated by a permanent magnet and washed several times by



165 deionized water, and then dried at 80°C. The obtained sample was denoted as g-  
 166 C<sub>3</sub>N<sub>4</sub>/Fe<sub>3</sub>O<sub>4</sub>/Ag<sub>3</sub>PO<sub>4</sub>@Sep. **Figure. 3** shows the steps involved in the magnetic g-  
 167 C<sub>3</sub>N<sub>4</sub>/Fe<sub>3</sub>O<sub>4</sub>/Ag<sub>3</sub>PO<sub>4</sub>@Sep nanocomposite synthesis.

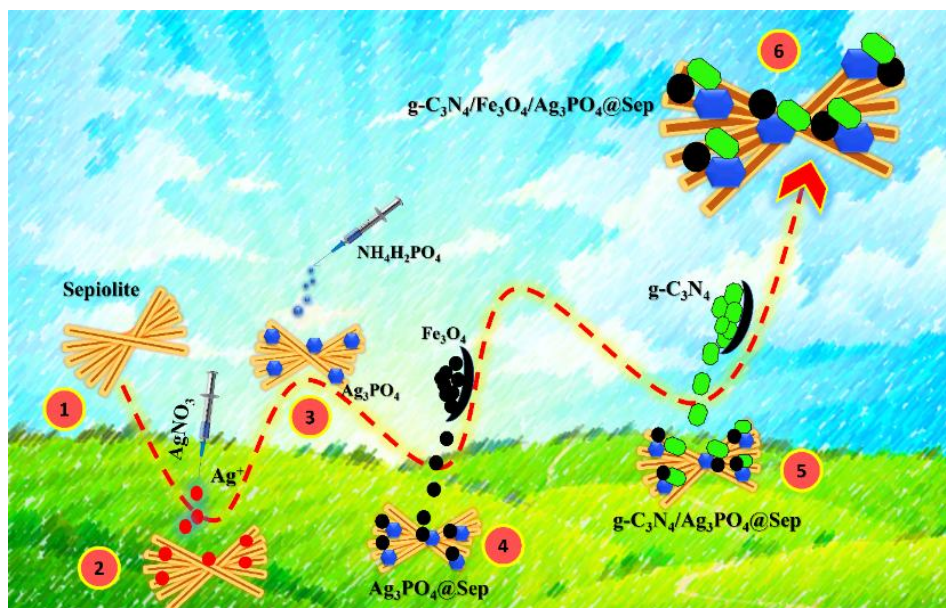


**Figure. 3:** The formation mechanism of quaternary g-C<sub>3</sub>N<sub>4</sub>/Fe<sub>3</sub>O<sub>4</sub>/Ag<sub>3</sub>PO<sub>4</sub>@Sep

168

## 169 2.2. Photocatalytic activity

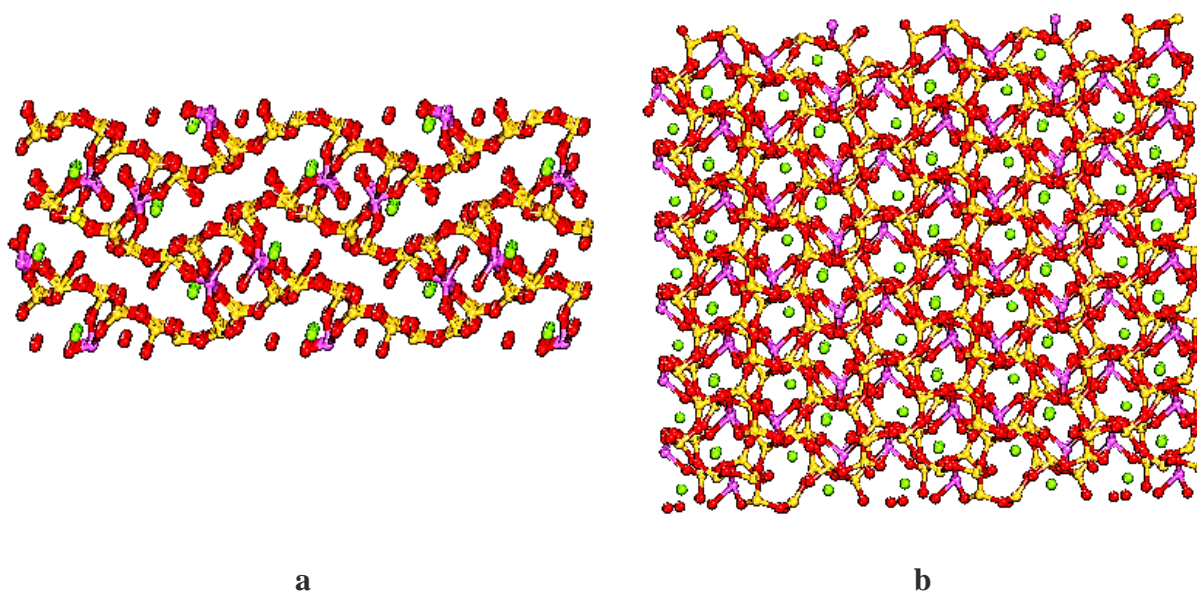
170 The photocatalytic activity of the g-C<sub>3</sub>N<sub>4</sub>, Ag<sub>3</sub>PO<sub>4</sub>, Fe<sub>3</sub>O<sub>4</sub>, Ag<sub>3</sub>PO<sub>4</sub>@Sep and g-  
 171 C<sub>3</sub>N<sub>4</sub>/Fe<sub>3</sub>O<sub>4</sub>/Ag<sub>3</sub>PO<sub>4</sub>@Sep nanocomposite photocatalysts were evaluated for the  
 172 photodegradation of Malachite Green (MG) in aqueous media under sunlight irradiation.  
 173 Hence, in typical photocatalytic experiment, an amount of 100 mg of the photocatalyst was  
 174 dispersed in 100 mL MG dye solution (10 mg/L). The prepared suspensions were maintained  
 175 inside the reactor, in the dark, for 1 h to reach an adsorption-desorption equilibrium between  
 176 the support and MG dye molecules, then 5 mL solutions were withdrawn every 2 minutes  
 177 under sunlight irradiation. Subsequently, the solution was centrifuged to separate the liquid  
 178 and solid phases for determine the concentration of MG dye with the wavelength of 615 nm  
 179 using UV visible JENWAY-6705 spectrophotometer. The percent degradation was measured  
 180 using the expression (**Eq.1**):

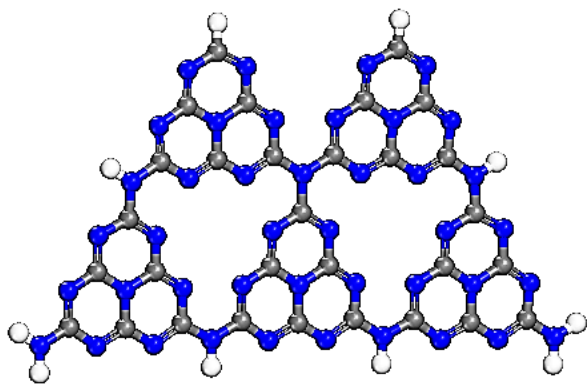
$$181 \quad \% \text{ of dye degradation} = \frac{C_0 - C_t}{C_0} \times 100 \quad (1)$$

182 where  $C_0$  is the original absorbance value of MG dye at initial time, and  $C_t$  is the absorbance  
 183 value of MG dye at a given time after sunlight irradiation.

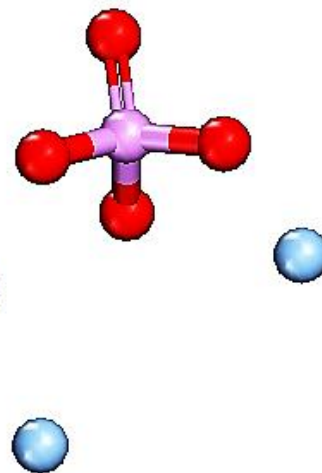
184 **2.3. Computational details**

185  $\text{Mg}_4\text{Si}_6\text{O}_{15}(\text{OH})_2 \cdot 6\text{H}_2\text{O}$  (sepiolite like palygorskite: Sep) with lattice parameters  $a = 13.5$ ,  $b =$   
186  $27.0$ , and  $c = 5.30 \text{ \AA}$  and built based on (200) surface and thickness of  $1.574 \text{ \AA}$  (**Figures 4a-b**)  
187 [21].  $\text{C}_3\text{N}_4$ ,  $\text{Ag}_3\text{PO}_4$  and MG (malachite green) was used to perform all the required  
188 calculations based on Density functional theory (DFT-D) by DMol<sup>3</sup> module, GGA/ PBE  
189 functional and DND and spin-unrestricted in Materials Studio 2017 software (**Figures 4c-d**).  
190  $\text{Fe}_3\text{O}_4$  as cubic (ID: mp-753222 and Point Group  $\text{Fd}\bar{3}\text{m}$ ) with  $a = b = c = 8.44 \text{ \AA}$ ,  $\alpha = \beta = \gamma =$   
191  $90.00^\circ$  and volume of  $602.06 \text{ \AA}^3$  was downloaded from  
192 <https://materialsproject.org/materials/mp-19306> (Figures 4e-f). After that,  $\text{Fe}_3\text{O}_4$  without  
193 unitcell was made based on (220) surface and thickness of  $1.500 \text{ \AA}$  and slab position (1.00)  
194 (**Figure 4g**). In order construct nano-composite  $\text{Fe}_3\text{O}_4/\text{Ag}_3\text{PO}_4@\text{Sep}$ , dynamic calculation (by  
195 the Monte Carlo adsorption locator module) was used to assess the adsorption of 6  $\text{C}_3\text{N}_4$ ,  
196  $\text{Ag}_3\text{PO}_4$  and  $\text{Fe}_3\text{O}_4$  molecules [22]. Additionally, 6 molecules of MG were adsorbed on  
197  $\text{Ag}_3\text{PO}_4(\text{Ag}_3\text{PO}_4@\text{Sep})$  by the Monte Carlo adsorption locator module [23].

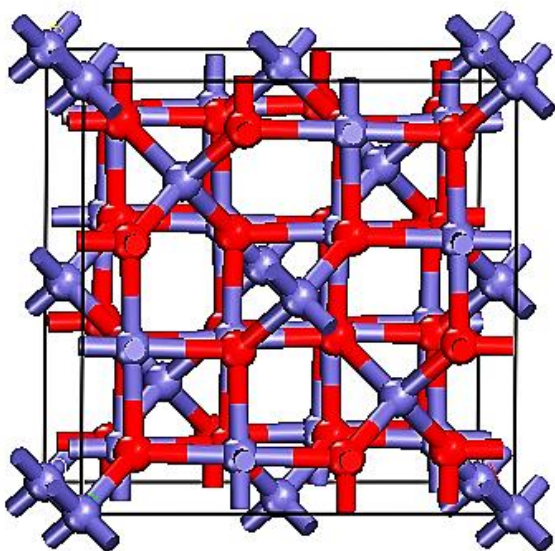




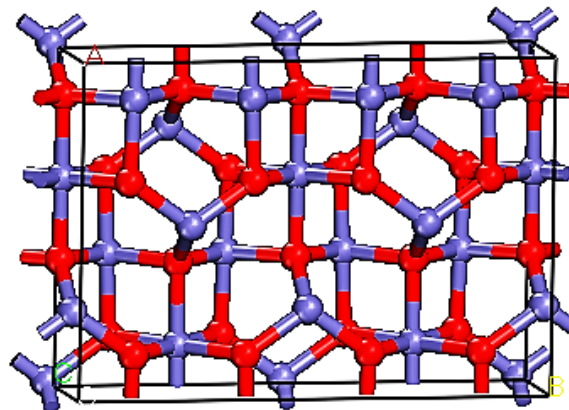
c



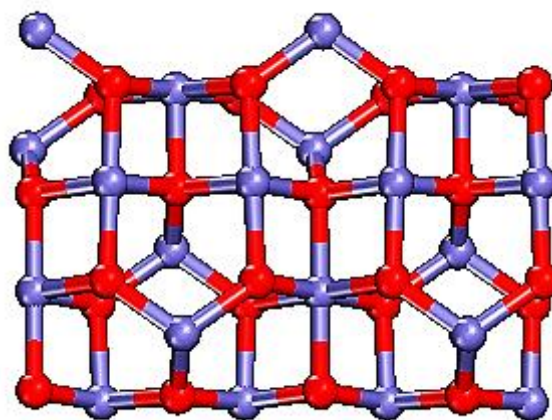
d



e



f



g

**Figure 4.** Snapshots of the optimized structures (a and b);  $\text{Mg}_4\text{Si}_6\text{O}_{15}(\text{OH})_2 \cdot 6\text{H}_2\text{O}$  (sepiolite,

(c); C<sub>3</sub>N<sub>4</sub>, (d); Ag<sub>3</sub>PO<sub>4</sub>, (e); Fe<sub>3</sub>O<sub>4</sub> as cubic (ID: mp-753222), (f); Fe<sub>3</sub>O<sub>4</sub> (220) and (g); Fe<sub>3</sub>O<sub>4</sub> (220) without unicell. Colored balls are Mg (green), oxygen (red), orange (Si), violet (Fe), pink (Al), and white (H).

198

### 199 3. Results and discussion

#### 200 3.1. Characterizations of the g-C<sub>3</sub>N<sub>4</sub>/Fe<sub>3</sub>O<sub>4</sub>/Ag<sub>3</sub>PO<sub>4</sub>@Sep nanocomposites

##### 201 *XRD analyzes*

202 The crystalline structures of the as-prepared samples were determined by XRD. Thus, **Figure.**  
203 **5** shows the XRD patterns of pure g-C<sub>3</sub>N<sub>4</sub>, sepiolite, Fe<sub>3</sub>O<sub>4</sub> and g-C<sub>3</sub>N<sub>4</sub>/Fe<sub>3</sub>O<sub>4</sub>/Ag<sub>3</sub>PO<sub>4</sub>@Sep  
204 nanocomposites.

205 Two distinct fundamental diffraction peaks are shown for the g-C<sub>3</sub>N<sub>4</sub> sample, the great peak  
206 located at ~ 27.4° corresponds to (0 0 2) planes and it is due to the stacking of the conjugated  
207 double bonds with the interlayer d-spacing (0.336 nm), while the small peak at~13.1°, is  
208 indexed as (1 0 0) planes, and it is attributed to the interplanar of interlayer d-spacing  
209 (0.672 nm) [24]. For the sepiolite clay, all the observed diffraction peaks of the sample were  
210 found to correspond to the JCPDS card (No. 75–1597) in addition to the observed few peaks  
211 resulting from quartz and carbonates impurities. The characteristic diffraction peaks of the  
212 synthesized Fe<sub>3</sub>O<sub>4</sub> nanoparticles occurred at diffraction angles, 2θ = 30.46°, 35.60°, 43.48°,  
213 53.84°, and 57.40°, which are attributed to (2 2 0), (3 1 1), (4 0 0), (4 2 2), and (5 1 1) planes,  
214 respectively, confirming the formation of the Fe<sub>3</sub>O<sub>4</sub> spinel cubic phase (JCPDS No. 01–076-  
215 0955). Finally, the X-ray diffraction (XRD) pattern of the g-C<sub>3</sub>N<sub>4</sub>/Fe<sub>3</sub>O<sub>4</sub>/Ag<sub>3</sub>PO<sub>4</sub>@Sep  
216 nanocomposite shows clearly all the diffraction peaks of Ag<sub>3</sub>PO<sub>4</sub> which can be easily indexed  
217 to the Ag<sub>3</sub>PO<sub>4</sub> centered cubic structure and correspond to the JCPDS card (No. 06-0505). As  
218 can be seen also in **Figure. 5**, the XRD spectrum of the nanocomposite shows the presence of  
219 the sepiolite and the body cubic spinel Fe<sub>3</sub>O<sub>4</sub> nanoparticles peaks, which confirm the  
220 successful preparation of g-C<sub>3</sub>N<sub>4</sub>/Fe<sub>3</sub>O<sub>4</sub>/Ag<sub>3</sub>PO<sub>4</sub>@Sep nanocomposite.

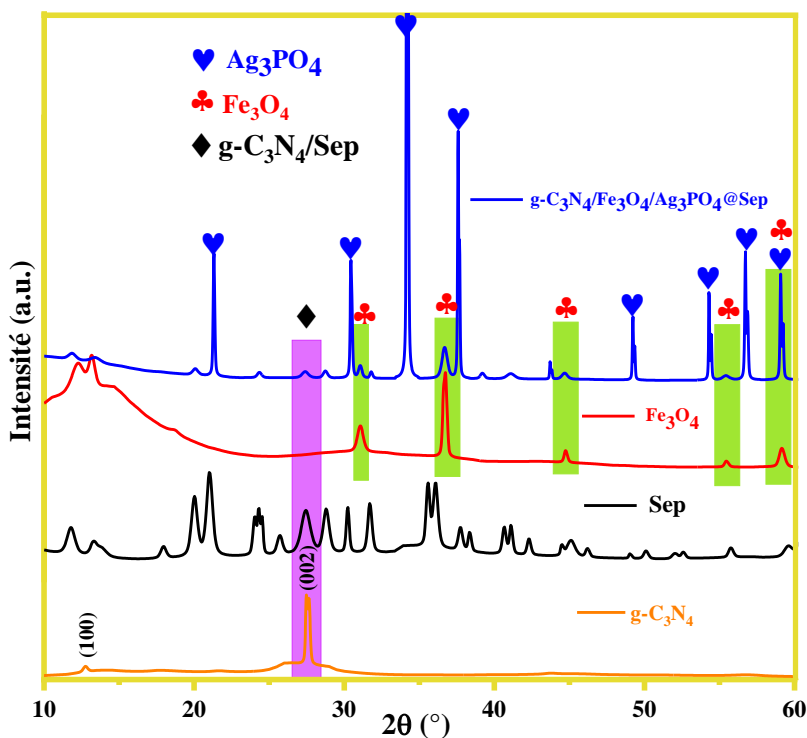


**Figure. 5.** XRD patterns of the prepared samples.

221

222 **FTIR analyzes**

223 In order to assess the successful formation of nanocomposites, FTIR spectroscopy was used  
 224 as a tool to investigate the chemical structures of the various prepared samples. Thus, **Figure.**  
 225 **6** shows the FTIR spectra of g-C<sub>3</sub>N<sub>4</sub>, Sepiolite, Fe<sub>3</sub>O<sub>4</sub>, Ag<sub>3</sub>PO<sub>4</sub>@Sep and g-  
 226 C<sub>3</sub>N<sub>4</sub>/Fe<sub>3</sub>O<sub>4</sub>/Ag<sub>3</sub>PO<sub>4</sub>@Sep catalysts. As can be seen in **Figure. 6a**, the g-C<sub>3</sub>N<sub>4</sub> sample shows  
 227 strong IR responses. In this figure, the bands located at 1251, 1325, 1419, 1571, and 1639 cm<sup>-1</sup>  
 228 <sup>1</sup> could be attributed to the typical stretching modes of CN heterocycles, whereas the  
 229 absorption peaks at 800 cm<sup>-1</sup> and 889 cm<sup>-1</sup> are ascribed to the typical breathing mode of tri-s-  
 230 triazine units and the deformation mode of N – H bonds, respectively [25, 26]. For the  
 231 sepiolite, the FTIR spectrum depicted in **Figure. 6b** exhibits two absorption peaks of zeolitic  
 232 water (3433 cm<sup>-1</sup> and 1644 cm<sup>-1</sup>) and coordinated water (3581 cm<sup>-1</sup>) present in the sepiolite  
 233 nanofibers structure. Note that the absorption peaks located in the region of 788–675 cm<sup>-1</sup>,  
 234 were attributed to the bending and the stretching vibration of hydroxyl groups (Mg-OH),  
 235 whereas the band located at 1016 cm<sup>-1</sup>, 455 cm<sup>-1</sup>, 1215 cm<sup>-1</sup> and 1074 cm<sup>-1</sup>, they might be  
 236 due to the Si-O bonds stretching[27, 28]. For the Fe<sub>3</sub>O<sub>4</sub> nanoparticles spectrum, as shown in  
 237 **Figure. 6c**, two characteristic peaks located at 556 cm<sup>-1</sup> and 1058 cm<sup>-1</sup> were observed,  
 238 corresponding to the Fe–O stretching mode in the Fe<sub>3</sub>O<sub>4</sub> confirming that the main phase is



239 magnetite[29]. In the case of  $\text{Ag}_3\text{PO}_4@\text{Sep}$ , as can be seen in **Figure. 6d**, the spectrum shows,  
 240 in addition to all characteristic peaks of raw sepiolite, three characteristic bands located at  
 241  $1012\text{ cm}^{-1}$ ,  $1012\text{ cm}^{-1}$  and  $1390\text{ cm}^{-1}$ , due to stretching vibration and bending vibration of P-  
 242 O-P and P=O of pure  $\text{Ag}_3\text{PO}_4$ [29].

243 For the  $\text{g-C}_3\text{N}_4/\text{Fe}_3\text{O}_4/\text{Ag}_3\text{PO}_4@\text{Sep}$  nanocomposite FTIR spectrum shown in **Figure. 6e**, as  
 244 can be observed, the presence of all the characteristic bands of sepiolite,  $\text{Fe}_3\text{O}_4$ ,  $\text{Ag}_3\text{PO}_4$  and  
 245  $\text{g-C}_3\text{N}_4$ , confirms that  $\text{Ag}_3\text{PO}_4$  nanoparticles cover the sepiolite surface of and they are joined  
 246 to the  $\text{g-C}_3\text{N}_4$  nano sheets by  $\text{Fe}_3\text{O}_4$  nanoparticles. Thus, from the overall FTIR data, the  
 247 successful preparation of the  $\text{g-C}_3\text{N}_4/\text{Fe}_3\text{O}_4/\text{Ag}_3\text{PO}_4@\text{Sep}$  nanocomposite is clearly  
 248 evidenced.

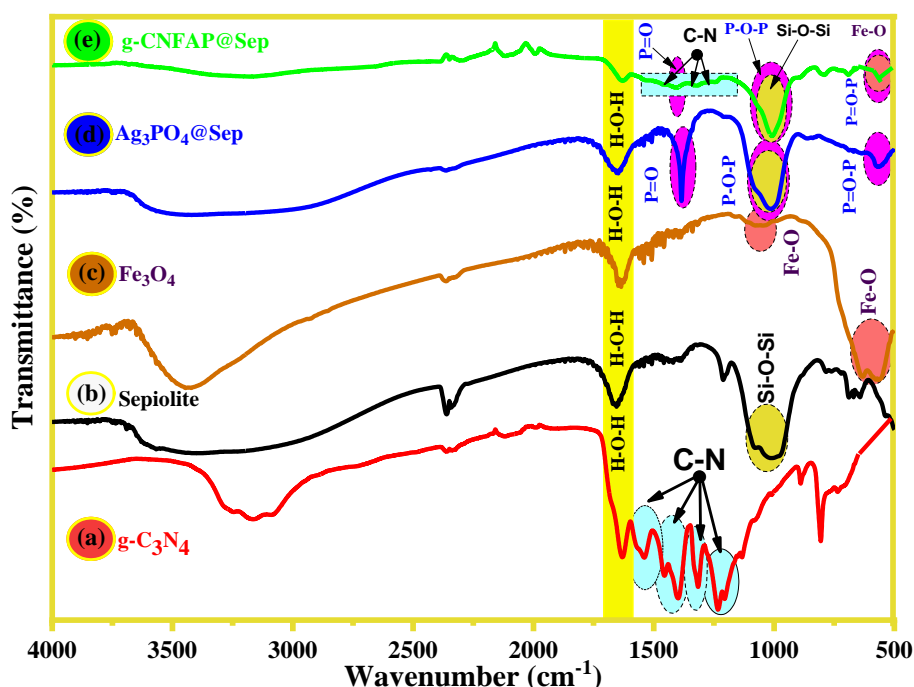


**Figure. 6.** FTIR spectra of photocatalysts. (a)  $\text{g-C}_3\text{N}_4$ , (b) Sepiolite, (c)  $\text{Fe}_3\text{O}_4$ , (d)  $\text{Ag}_3\text{PO}_4/\text{Sep}$  and (e)  $\text{g-C}_3\text{N}_4/\text{Fe}_3\text{O}_4/\text{Ag}_3\text{PO}_4@\text{Sep}$ .

249

### 250 *SEM analyzes*

251 The surface structure and morphological characteristics of  $\text{g-C}_3\text{N}_4$ , Sepiolite,  $\text{Ag}_3\text{PO}_4@\text{Sep}$   
 252 and  $\text{g-C}_3\text{N}_4/\text{Fe}_3\text{O}_4/\text{Ag}_3\text{PO}_4@\text{Sep}$  the composites were investigated using SEM as shown in  
 253 **Figure.7**. The  $\text{g-C}_3\text{N}_4$  (**Figure. 7a**) prepared directly from the calcination of the melamine  
 254 shows a mesoporous structure with an irregular sheet shape. It can be observed from **Figure.**  
 255 **7b** that the raw sepiolite surface reveals compact nodular with non-uniform fibrous filament

256 morphology. After surface modification of sepiolite by  $\text{Ag}_3\text{PO}_4$  nanoparticles, as shown in  
 257 **Figure. 7c**, it is obvious that the  $\text{Ag}_3\text{PO}_4$  slightly changes the raw sepiolite by making the  
 258 nanofibrous surface rougher. Note that the  $\text{Ag}_3\text{PO}_4$  nanoparticles attachment on the sepiolite  
 259 surface results from the electrostatic interaction. In addition, the image in **Figure. 7c** shows  
 260 small particle sizes with sheets shapes, which are attributed to  $\text{g-C}_3\text{N}_4$ . According to the SEM  
 261 image of  $\text{g-C}_3\text{N}_4/\text{Fe}_3\text{O}_4/\text{Ag}_3\text{PO}_4@\text{Sep}$  nanocomposite shown in **Figure. 7d**, the  $\text{Fe}_3\text{O}_4$   
 262 nanoparticles, the  $\text{Ag}_3\text{PO}_4$  nanoscale and the  $\text{g-C}_3\text{N}_4$  nanosheets are homogeneously  
 263 distributed, and cover all the sepiolite fibrous surface. In summary, the obtained SEM images  
 264 show high adhesion of the prepared catalysts, mainly  $\text{Ag}_3\text{PO}_4$  particles on the sepiolite surface,  
 265 which may increase the nano composite photogenerated carriers' lifetime.

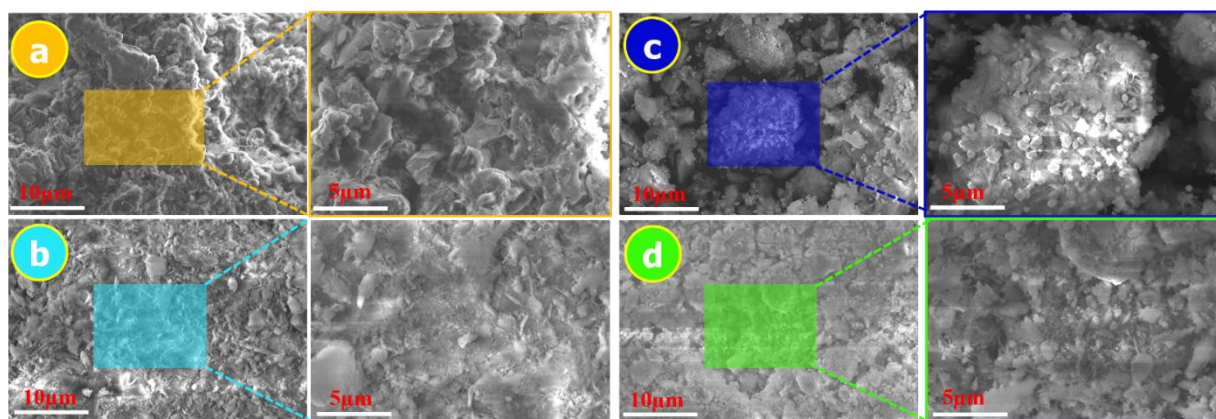


**Figure. 7.** SEM images of  $\text{g-C}_3\text{N}_4$  (a), sepiolite (b),  $\text{g-C}_3\text{N}_4/\text{Ag}_3\text{PO}_4@\text{Sep}$  (c) and  $\text{g-C}_3\text{N}_4/\text{Fe}_3\text{O}_4/\text{Ag}_3\text{PO}_4@\text{Sep}$  (d).

266

### 267 *EDX and mapping analyzes*

268 The energy dispersive X-ray spectra (EDX) and the mapping are two of the effective methods  
 269 for determining the sample chemical composition and its purity. The EDX spectra and image  
 270 mapping of the synthesized samples,  $\text{g-C}_3\text{N}_4$ , sepiolite,  $\text{Ag}_3\text{PO}_4@\text{Sep}$  and  $\text{g-C}_3\text{N}_4/\text{Fe}_3\text{O}_4/\text{Ag}_3\text{PO}_4@\text{Sep}$   
 271 nanocomposite are displayed in **Figure. 8a-d**. The spectrum for the  $\text{g-C}_3\text{N}_4$  shows, as expected, the presence of C and N elements. Similarly, the raw sepiolite  
 272 EDX spectrum shown in **Figure. 8b**, indicates the presence in the sample of the O, Mg and Si  
 273 elements. Moreover, the EDX spectrum of  $\text{g-C}_3\text{N}_4/\text{Ag}_3\text{PO}_4@\text{Sep}$  nanocomposite shows that  
 274 all the elements in the nanocomposite are found to be matched such as O, Mg, Si, C, N, Ag  
 275 and P. The EDX spectrum of  $\text{g-C}_3\text{N}_4/\text{Fe}_3\text{O}_4/\text{Ag}_3\text{PO}_4@\text{Sep}$  nanocomposite indicates the  
 276 appearance of O, Mg, Si, C, N, Ag, P and Fe elements, and the mapping shows that the g-

278  $C_3N_4$ ,  $Ag_3PO_4$ , and  $Fe_3O_4$  elements, are homogeneously distributed on the sepiolite surface.  
 279 **Table 1** is presented the atomic percentages of different elements.

280

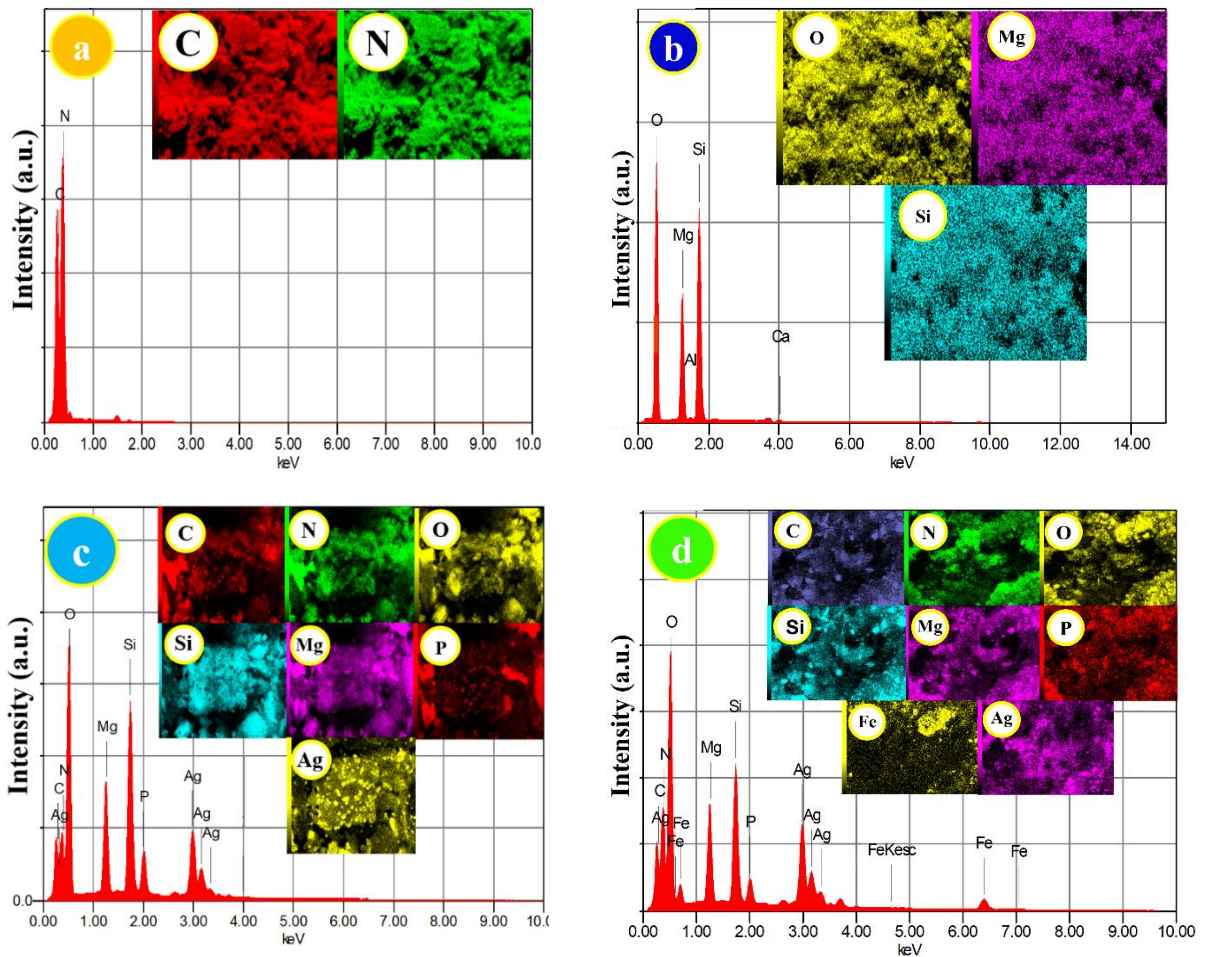


**Figure.8.** EDX spectra and mapping micrographs, of  $g-C_3N_4$ (a), sepiolite (b),  $g-C_3N_4/Ag_3PO_4@Sep$  (c) and  $g-C_3N_4/Fe_3O_4/Ag_3PO_4@Sep$  (d).

281

282 **TEM analyzes**

283 Transmission electron microscopy (TEM) is an excellent analytical method in the physical,  
 284 chemical, sciences can be used to find the morphology and size of different materials. In this  
 285 study, TEM analysis was used to investigate the particle size and morphology of  $g-C_3N_4$ ,  $g-$   
 286  $C_3N_4/sepiolite$ ,  $g-C_3N_4/Ag_3PO_4$  and  $g-C_3N_4/Fe_3O_4/Ag_3PO_4@Sep$  nanocomposites in details.  
 287 As shown in **Figure. 9a**, the pristine  $g-C_3N_4$  have uniform fabric-like folded nanosheets  
 288 fabric-like folded nanosheets with thin thickness porous. The porous structure was favorable



289 for the catalyst to absorb pollutants and further promote the degradation and was in the size  
 290 range of about 50-80 nm.

291 **Table 1.** Atomic percentages of the g-C<sub>3</sub>N<sub>4</sub>, sepiolite, g-C<sub>3</sub>N<sub>4</sub>/Ag<sub>3</sub>PO<sub>4</sub>@Sep and the g-  
 292 C<sub>3</sub>N<sub>4</sub>/Fe<sub>3</sub>O<sub>4</sub>/Ag<sub>3</sub>PO<sub>4</sub>@Sep elements.

		C	N	O	Mg	Si	Ag	P	Fe	Ca	Al
<b>g-C<sub>3</sub>N<sub>4</sub></b>	At	44.59	55.41	-	-	-	-	-	-	-	-
	%										
<b>Sepiolite</b>	At	-	-	63.56	20.25	15.56	-	-	-	0.4	0.
	%									3	2
<b>g-C<sub>3</sub>N<sub>4</sub>/Ag<sub>3</sub>PO<sub>4</sub>@Sep</b>	At	8.82	4.33	45.35	8.29	21.06	10.13	2.02	-	-	-
	%										
<b>C<sub>3</sub>N<sub>4</sub>/Fe<sub>3</sub>O<sub>4</sub>/Ag<sub>3</sub>PO<sub>4</sub>@ Sep</b>	At	9.42	12.02	41.01	7.83	19.04	6.35	2.22	2.1	-	-
	%										

293

294 The corresponding TEM image of g-C<sub>3</sub>N<sub>4</sub>/sepiolite is given in **Figure. 9b**. It reveals that the  
 295 sepiolite shows nanotubes-like fibers having uniform diameters with an average of ~ 30 nm,  
 296 which exhibited the strong contact between nanosheets g-C<sub>3</sub>N<sub>4</sub>. The **Figure. 9c** is clearly  
 297 displayed the strong interfacial contact between g-C<sub>3</sub>N<sub>4</sub> and Ag<sub>3</sub>PO<sub>4</sub>, which is conducive to  
 298 the rapid transfer and separation of photogenerated electron–hole pairs in g-C<sub>3</sub>N<sub>4</sub>/ Ag<sub>3</sub>PO<sub>4</sub>  
 299 nanocomposite. Moreover, the Ag<sub>3</sub>PO<sub>4</sub> exhibited hexagonal form with a size of ~ 200 nm. In  
 300 addition, it could be observed from the **Figure. 9d** that all as prepared catalysts nanoparticles  
 301 g-C<sub>3</sub>N<sub>4</sub>, Ag<sub>3</sub>PO<sub>4</sub> and Fe<sub>3</sub>O<sub>4</sub>were homogeneously loaded on the nanotubes sepiolite surface.  
 302 Even more important, the photocatalysts g-C<sub>3</sub>N<sub>4</sub> and Ag<sub>3</sub>PO<sub>4</sub> are implying the strong  
 303 interfacial contact between them by Fe<sub>3</sub>O<sub>4</sub> nanoparticles, which may favor the charge transfer.  
 304 So, the obtained results reinforce what was previously obtained by several analysis  
 305 techniques.

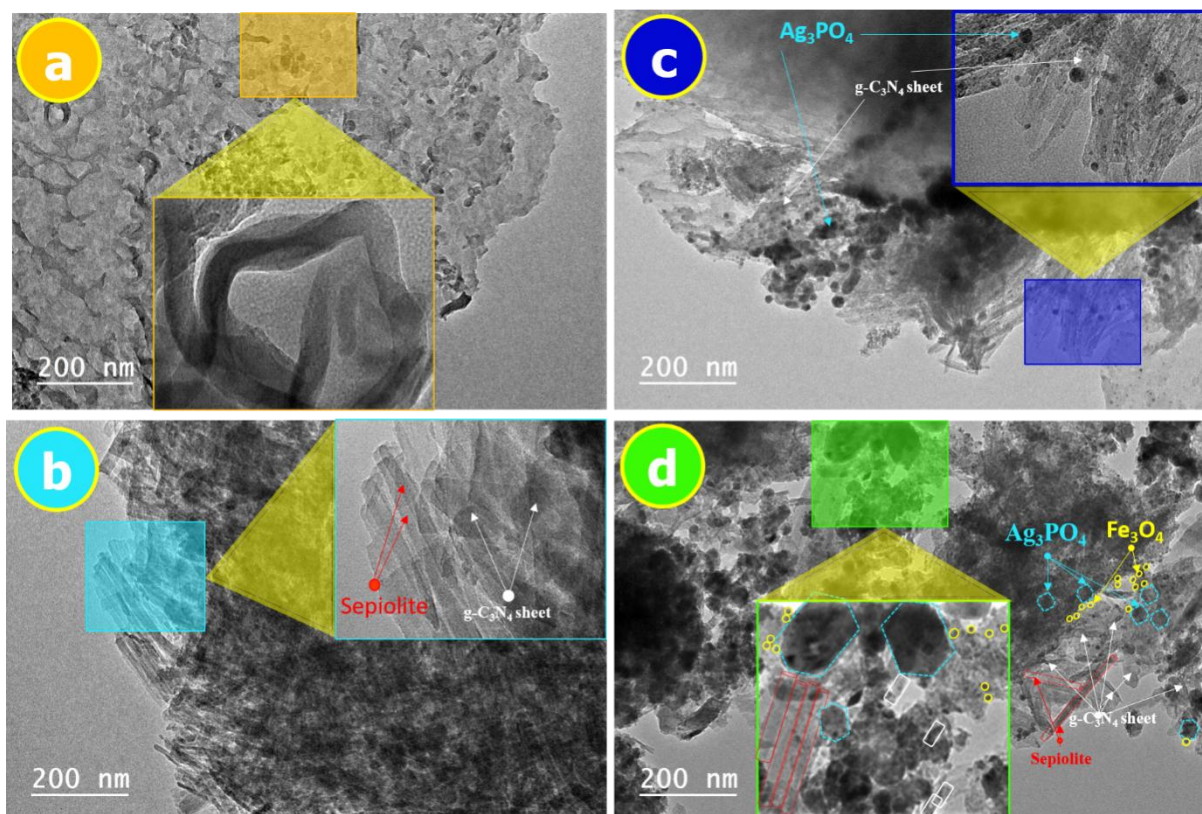


**Figure. 9.** TEM images of the  $g\text{-C}_3\text{N}_4$  (a),  $g\text{-C}_3\text{N}_4/\text{sepiolite}$  (b),  $g\text{-C}_3\text{N}_4/\text{Ag}_3\text{PO}_4$  (d) and  $\text{C}_3\text{N}_4/\text{Fe}_3\text{O}_4/\text{Ag}_3\text{PO}_4@\text{Sep}$

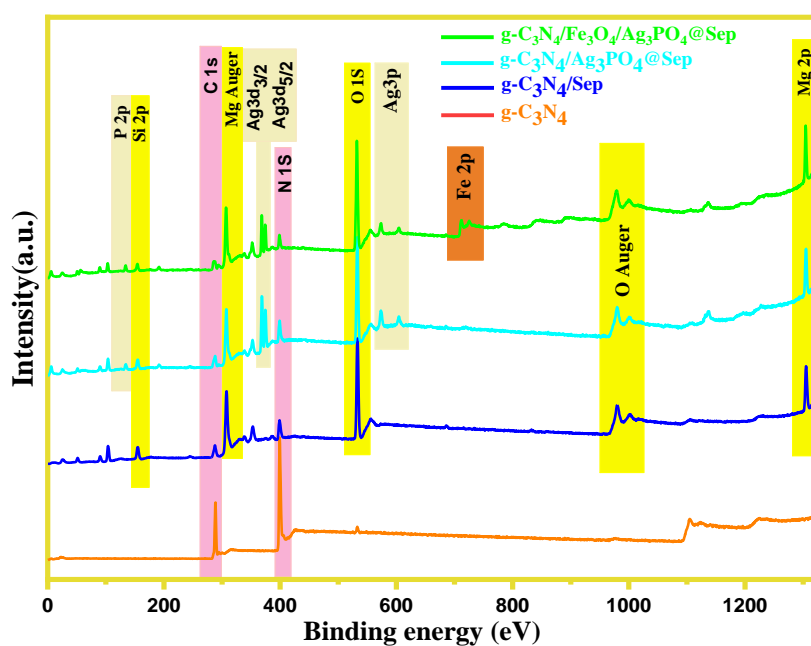
306

### 307 *XPS analyzes*

308 XPS is commonly quantitative technique used to provide information on the elemental  
 309 composition and the valence states of constituent elements on the surface of the  
 310 nanomaterials. Nevertheless, the chemical species in the surface of  $g\text{-C}_3\text{N}_4$ ,  $g\text{-C}_3\text{N}_4/\text{sepiolite}$ , -  
 311  $\text{C}_3\text{N}_4/\text{Ag}_3\text{PO}_4 / \text{Sep}$  and  $g\text{-C}_3\text{N}_4/\text{Fe}_3\text{O}_4/\text{Ag}_3\text{PO}_4@\text{Sep}$  nanocomposites were confirmed by XPS  
 312 and reported in **Figure.10**. The XPS spectrum of  $g\text{-C}_3\text{N}_4$  **10a** reveals mainly two peaks  
 313 assigned to C1s and N1s, the spectrum of  $g\text{-C}_3\text{N}_4/\text{sepiolite}$  **Figure. 10a** shows seven main  
 314 elements C 1s, N 1s, Si 2p, O 1s, Mg 2p, O Auger and Mg Auger. Moreover, the spectrum of  
 315  $g\text{-C}_3\text{N}_4/\text{Ag}_3\text{PO}_4$  (**Figure. 10a**) includes all peaks of  $g\text{-C}_3\text{N}_4$  and sepiolite as well as four  
 316 elements P2p, Ag 3d<sub>3/2</sub>, Ag 3d<sub>5/2</sub> and Ag3p. The XPS spectrum of  $g\text{-C}_3\text{N}_4/\text{Fe}_3\text{O}_4/\text{Ag}_3\text{PO}_4@\text{Sep}$   
 317 nanocomposite is reported in **Figure. 10a**, it can be seen that all peaks of  $g\text{-C}_3\text{N}_4$ , sepiolite  
 318 and  $\text{Ag}_3\text{PO}_4$  are existing as well as element Fe 2p, which confirm the presence of  $\text{Fe}_3\text{O}_4$  in the  
 319 surface of sepiolite. **Figure.10b** shows the high-resolution XPS spectra of the peak of Si 2p  
 320 located in the region of 101.97 eV, which revealing the valence state of the silicon.

321 **Figure.10c** detects the deconvoluted Mg 2s spectra located at 1303.2 eV, which can be  
 322 attributed to magnesium hydroxides Mg-OH. In **Figure. 10d**, the C 1s spectrum can be  
 323 decomposed into two constituents at 284.8 and 288.3 eV for the C-C and C-N chemical  
 324 bonding, respectively[30, 31].The N 1s peak of g-C<sub>3</sub>N<sub>4</sub> could be deconvoluted into three  
 325 Gaussian–Lorentzian fitted peaks at 398.96, 399.67, and 400.9 eV, which were attributed to  
 326 pyridinic N (C-N=C), pyrrolic N (N-(C)<sub>3</sub>), and graphitic N (C-N-H) respectively (**Figure. 10e**  
 327 ) [32, 33].The deconvoluted Ag3d spectra demonstrate the existence of two main peaks at  
 328 367.2 and 373.17 eV (**Figure. 10f**), assigned to the Ag3d<sub>5/2</sub> and Ag3d<sub>3/2</sub> of Ag<sup>+</sup> in the  
 329 nanocomposite. The deconvolution of O1s from the nanocomposite display two principal  
 330 peaks at 531.1 and 532.32 eV, corresponding to and the lattice oxygen atoms (O<sup>2-</sup>) and H<sub>2</sub>O  
 331 molecules adsorbing on the surface of nanocomposite **Figure. 10g** [34, 35]. Deconvolution Fe  
 332 2p orbital presents two main spectrum located at 711.97 and 725.56 eV, could be due to the  
 333 Fe 2p<sub>3/2</sub> and Fe 2p<sub>1/2</sub> spin orbitals of magnetite, respectively, **Figure. 10h** [36].As can be  
 334 seen in **Figure 10.i**. the peak at 132.8eV may be attributed to the P2p, which is assigned to  
 335 P<sup>5+</sup> of PO<sub>4</sub><sup>3-</sup> [36]. Therefore, these results could confirm the coexistence of g-C<sub>3</sub>N<sub>4</sub>, Ag<sub>3</sub>PO<sub>4</sub>  
 336 and Fe<sub>3</sub>O<sub>4</sub> in the g-C<sub>3</sub>N<sub>4</sub>/Fe<sub>3</sub>O<sub>4</sub>/Ag<sub>3</sub>PO<sub>4</sub>@Sep nanocomposites, and then create an important  
 337 synergistic effect during the photocatalytic activity.

338



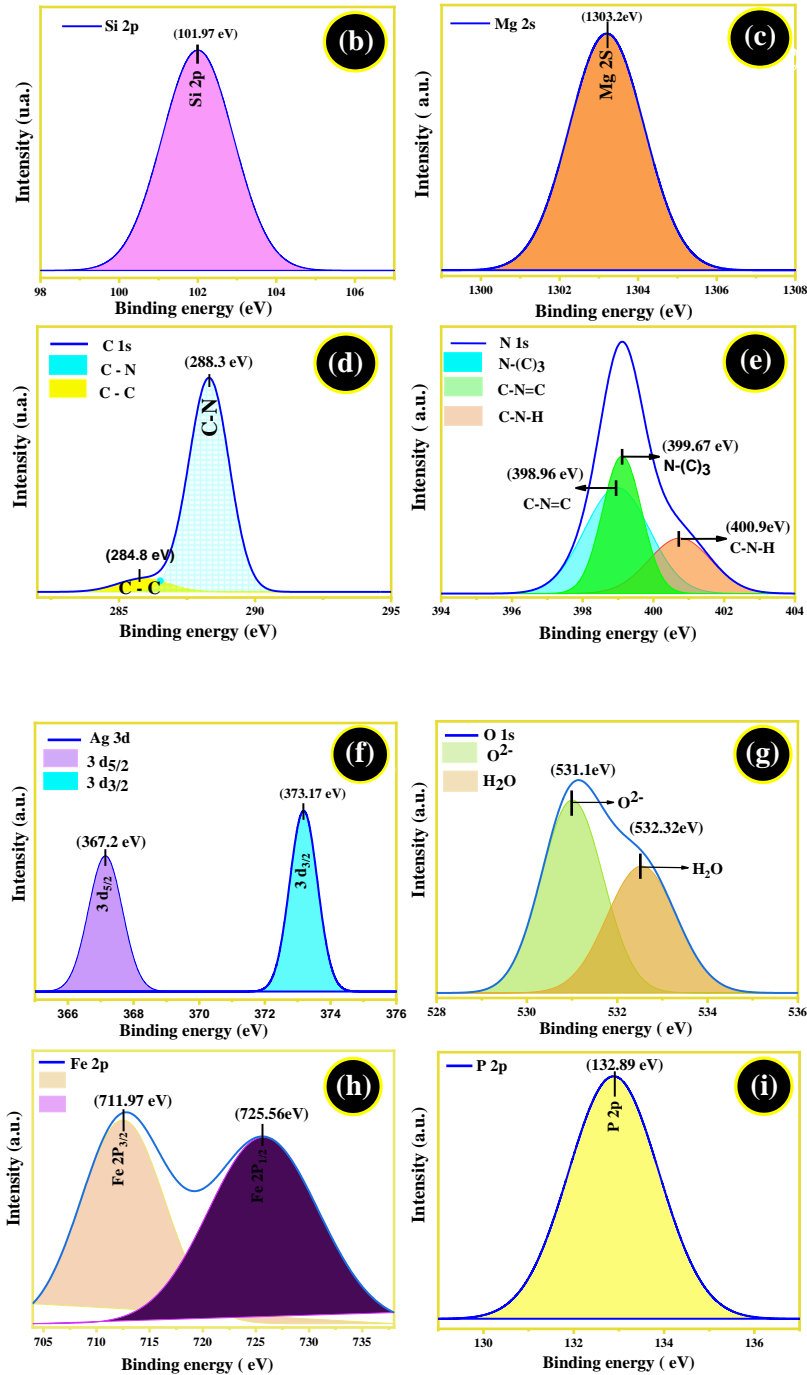


**Figure. 10.** XPS analyzes of g-C<sub>3</sub>N<sub>4</sub>, g-C<sub>3</sub>N<sub>4</sub>/Sep, g-C<sub>3</sub>N<sub>4</sub>/Ag<sub>3</sub>PO<sub>4</sub>@Sep and g-C<sub>3</sub>N<sub>4</sub>/Fe<sub>3</sub>O<sub>4</sub>/Ag<sub>3</sub>PO<sub>4</sub>@Sep nanocomposite (a) HR Si 2p spectrum (b) HR Mg 2s and (c) HR C 1s (d)HR N1s (e) HR Ag 3d (f)HR O1s (g) HR Fe 2p (h) HR P 2p (i).

339 **DRS analyzes**

340 Solid-state UV-Vis or diffuse reflectance spectroscopy (DRS) is a very useful technique to  
 341 investigate the electronic and optical properties of catalysts samples. It can be observed from

342 **Figure.11a** that all samples exhibited good light capture in the range of 200 to 500 nm, the  
 343 DRS spectrum shows an absorption band edge at  $\lambda$  440 nm corresponding to intrinsic  
 344 absorption of g-C<sub>3</sub>N<sub>4</sub> and Ag<sub>3</sub>PO<sub>4</sub> demonstrated an absorption band edge at  $\lambda$ 450 nm. When  
 345 Ag<sub>3</sub>PO<sub>4</sub>, g-C<sub>3</sub>N<sub>4</sub> and Fe<sub>3</sub>O<sub>4</sub> were supported on sepiolite, the optical absorption range was  
 346 broader, and the optical absorption intensity over the whole range of 200 -600 nm. This  
 347 indicates that Ag<sub>3</sub>PO<sub>4</sub>, g-C<sub>3</sub>N<sub>4</sub>, Fe<sub>3</sub>O<sub>4</sub> and sepiolite have a synergistic effect. Thus, the  
 348 increase in the absorption of g-C<sub>3</sub>N<sub>4</sub>/Fe<sub>3</sub>O<sub>4</sub>/Ag<sub>3</sub>PO<sub>4</sub>@Sep nanocomposite indicates that the  
 349 nanocomposite may demonstrate a remarkable photocatalytic activity in the visible region.

350 The band gaps of three samples can be calculated according to the Kubelka-Munk formula,  
 351 which is the following (Eq.2)[37, 38]:

$$352 \quad \alpha h\nu = A(h\nu - E_g)^{n/2} \quad (2)$$

353 Where  $\alpha$  is the absorption coefficient, h is Planck's constant,  $\nu$  is the frequency of light,  $E_g$   
 354 represents the band gap energy, A is a constant and n refers to the type of electron  
 355 transition.**Figure. 11b** shows  $(\alpha h\nu)^2$  versus energy (h $\nu$ ) diagrams of the band gap energy of g-  
 356 C<sub>3</sub>N<sub>4</sub>, Ag<sub>3</sub>PO<sub>4</sub> and g-C<sub>3</sub>N<sub>4</sub>/Fe<sub>3</sub>O<sub>4</sub>/Ag<sub>3</sub>PO<sub>4</sub>@Sep. As illustrated by the Tauc plot in **Figure.**  
 357 **11b** the band gap energies of g-C<sub>3</sub>N<sub>4</sub>, Ag<sub>3</sub>PO<sub>4</sub> and g-C<sub>3</sub>N<sub>4</sub>/Fe<sub>3</sub>O<sub>4</sub>/Ag<sub>3</sub>PO<sub>4</sub>@Sep are 2.94, 2.44  
 358 and 2.83 eV, respectively. So, the narrow band gap of the g-C<sub>3</sub>N<sub>4</sub>/Fe<sub>3</sub>O<sub>4</sub>/Ag<sub>3</sub>PO<sub>4</sub>@Sep  
 359 nanocomposite due to the existence of synergistic effect between sepiolite, Ag<sub>3</sub>PO<sub>4</sub>, g-C<sub>3</sub>N<sub>4</sub>  
 360 and Fe<sub>3</sub>O<sub>4</sub> shows that it has a higher visible light absorption ability, which could help in the  
 361 separation of electron-hole pairs.

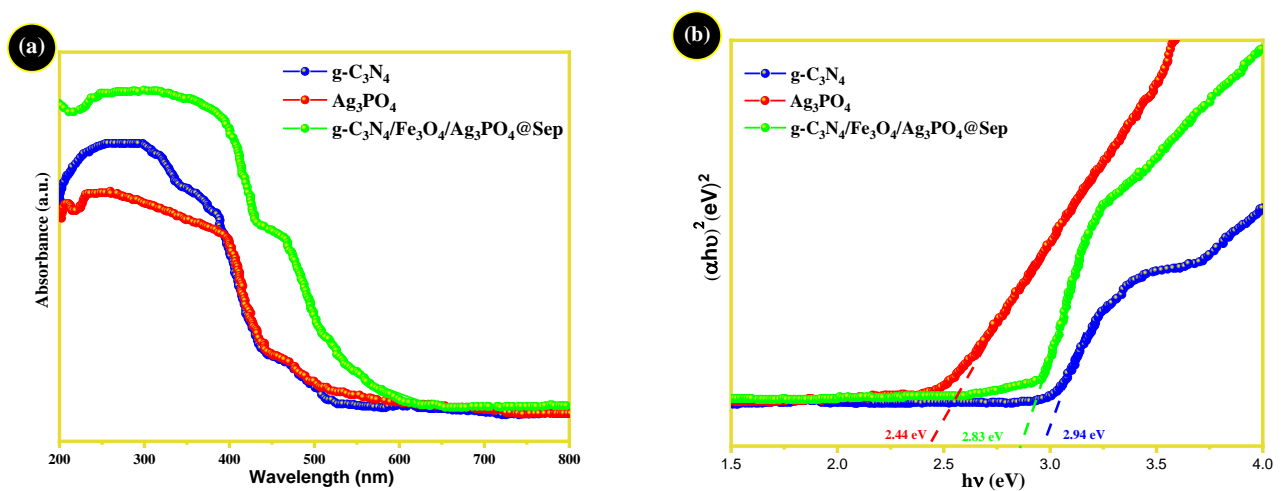


**Figure. 11.** (a) UV–Vis diffuse reflectance spectra and (b)Tauc plot of the prepared samples: g-C<sub>3</sub>N<sub>4</sub>, Ag<sub>3</sub>PO<sub>4</sub> and g-C<sub>3</sub>N<sub>4</sub>/Fe<sub>3</sub>O<sub>4</sub>/Ag<sub>3</sub>PO<sub>4</sub>@Sep.

362

### 363 3.2. Photocatalytic activity of g-C<sub>3</sub>N<sub>4</sub>/Fe<sub>3</sub>O<sub>4</sub>/Ag<sub>3</sub>PO<sub>4</sub>@Sep nanocomposite

364 The photocatalytic activities of all synthesized photocatalysts were examined by degradation  
365 of MG dye under sunlight irradiation to study their potential applicability in the field of  
366 environmental treatment.

367 Firstly, the photodegradation of MG without catalyst was studied for comparison (i. e. MG  
368 aqueous solution irradiated with sunlight in the absence of the photocatalyst). In the absence  
369 of the photocatalyst (**Figure. 12a**), the results indicate that no degradation of MG was  
370 observed after 12 minutes of irradiation. This indicated that MG dye is not effectively  
371 decontaminated by photolysis alone (i.e. under sunlight irradiation and in the absence of the  
372 photocatalyst). In the other hand, as can be seen in **Figure. 12a**, in the absence of Sunlight  
373 irradiation, the adsorption of MG from water onto the prepared catalyst surfaces, such as, g-  
374 C<sub>3</sub>N<sub>4</sub>, g-C<sub>3</sub>N<sub>4</sub>/Sep, g-C<sub>3</sub>N<sub>4</sub>/Ag<sub>3</sub>PO<sub>4</sub>@Sep and g-C<sub>3</sub>N<sub>4</sub>/Fe<sub>3</sub>O<sub>4</sub>/Ag<sub>3</sub>PO<sub>4</sub>@Sep nanocomposites,  
375 were also investigated. It can be seen from **Figure. 12a** that the MG dye molecules were only  
376 slightly removed from water after 60 minutes. The removal efficiencies of the MG dye, in the  
377 absence of Sunlight irradiation, achieved approximately 13%, 10%, 7% and 2% for g-C<sub>3</sub>N<sub>4</sub>, g-  
378 C<sub>3</sub>N<sub>4</sub>/Ag<sub>3</sub>PO<sub>4</sub>@Sep, g-C<sub>3</sub>N<sub>4</sub>/Sep and g-C<sub>3</sub>N<sub>4</sub>/Fe<sub>3</sub>O<sub>4</sub>/Ag<sub>3</sub>PO<sub>4</sub>@Sep nanocomposite,  
379 respectively. These data indicate that all the synthesized photocatalysts show low adsorption  
380 activities towards the MG dye.

381 Besides, **Figure. 12b** shows the MG dye removal, under Sunlight irradiation, from aqueous  
382 media onto different types of prepared photocatalysts, including g-C<sub>3</sub>N<sub>4</sub>, g-C<sub>3</sub>N<sub>4</sub>/Sep, g-  
383 C<sub>3</sub>N<sub>4</sub>/Ag<sub>3</sub>PO<sub>4</sub>@Sep and g-C<sub>3</sub>N<sub>4</sub>/Fe<sub>3</sub>O<sub>4</sub>/Ag<sub>3</sub>PO<sub>4</sub>@Sep nanocomposite during the same period.  
384 The observed degradation efficiencies for MG dye are about  $\approx 23.91\%$ ,  $\approx 25.52\%$ ,  $\approx 76.55\%$   
385 and  $\approx 100\%$ , for the g-C<sub>3</sub>N<sub>4</sub>, g-C<sub>3</sub>N<sub>4</sub>/Sep, g-C<sub>3</sub>N<sub>4</sub>/Ag<sub>3</sub>PO<sub>4</sub>@Sep and g-  
386 C<sub>3</sub>N<sub>4</sub>/Fe<sub>3</sub>O<sub>4</sub>/Ag<sub>3</sub>PO<sub>4</sub>@Sep nanocomposite in the 12 min of irradiation, respectively.  
387 Obviously, the order of photocatalytic activity of the prepared photocatalysts is: g-  
388 C<sub>3</sub>N<sub>4</sub>/Fe<sub>3</sub>O<sub>4</sub>/Ag<sub>3</sub>PO<sub>4</sub>@Sep > g-C<sub>3</sub>N<sub>4</sub>/Ag<sub>3</sub>PO<sub>4</sub>@Sep > g-C<sub>3</sub>N<sub>4</sub>/Sep > g-C<sub>3</sub>N<sub>4</sub>. **Figure. 12b**  
389 shows clearly that the concentration of MG dye decreases dramatically, as time increases, and  
390 nearly disappears within only 16 min. So, the results obtained demonstrate that the  
391 photocatalytic activity of g-C<sub>3</sub>N<sub>4</sub>/Fe<sub>3</sub>O<sub>4</sub>/Ag<sub>3</sub>PO<sub>4</sub>@Sep nanocomposite towards MG dye, under  
392 sunlight irradiation, is higher in comparison to the others photocatalysts. Such difference in  
393 behaviour between g-C<sub>3</sub>N<sub>4</sub>/Fe<sub>3</sub>O<sub>4</sub>/Ag<sub>3</sub>PO<sub>4</sub>@Sep and the others catalysts, can be due to several

394 effects. Firstly, the magnetic nanocomposite exhibits high ability to absorb visible light.  
 395 Secondly, the synergistic effect occurring between the three samples: Ag<sub>3</sub>PO<sub>4</sub>, g-C<sub>3</sub>N<sub>4</sub> and  
 396 Fe<sub>3</sub>O<sub>4</sub>, leading to photoactivity enhancement. Thirdly, the high electrostatic interactions  
 397 occurring between the Ag<sub>3</sub>PO<sub>4</sub> nanoparticles and the sepiolite negative sites, lead to the  
 398 stability of Ag<sub>3</sub>PO<sub>4</sub> nanoparticles caused by the strong adhesion of Ag<sub>3</sub>PO<sub>4</sub> on the sepiolite  
 399 surface, improve the electrons and holes separation, and prevent their recombination.  
 400 Fourthly, the increase in the degradation efficiency is due to the availability of more active  
 401 sites in the g-C<sub>3</sub>N<sub>4</sub>/Fe<sub>3</sub>O<sub>4</sub>/Ag<sub>3</sub>PO<sub>4</sub>@Sep nanocomposite. Fifthly, the sepiolite was used as an  
 402 excellent support by increasing the contact between Ag<sub>3</sub>PO<sub>4</sub> and the solar-light photons.  
 403 Finally, the Fe<sub>3</sub>O<sub>4</sub> nanoparticles can be used as an efficient electron transfer compound  
 404 leading to recombination reduction of the photogenerated carriers and facilitating the transfer  
 405 of photogenerated electrons. Therefore, it can be concluded that the preparation of the  
 406 magnetic Z-heterojunction g-C<sub>3</sub>N<sub>4</sub>/Fe<sub>3</sub>O<sub>4</sub>/Ag<sub>3</sub>PO<sub>4</sub>@Sep should be used as a stronger  
 407 photocatalyst for the degradation of hazardous organic pollutants such as toxic dyes.  
 408 Furthermore, the photocatalytic performance of the magnetic nanocomposite prepared in the  
 409 present work, was evaluated and compared with other photocatalysts found in the literature  
 410 (**Table 2**). Besides, the experimental kinetic data for the MG dye photodegradation in the  
 411 presence of the g-C<sub>3</sub>N<sub>4</sub>/Fe<sub>3</sub>O<sub>4</sub>/Ag<sub>3</sub>PO<sub>4</sub>@Sep nanocomposite were assessed and compared to  
 412 the first-order Langmuir-Hinshelwood model. Thus, according to (**Eq. 3**) the apparent  
 413 degradation rate constant of the first-order reaction, **K<sub>app</sub>**, can be calculated from the plot of ln  
 414 (C<sub>0</sub>/C<sub>t</sub>) versus t. Knowing the **K<sub>app</sub>** value, the half-life **t<sub>1/2</sub>** value can also be determined  
 415 according to (**Eq. 4**):

$$416 \quad \ln \left( \frac{C_0}{C_t} \right) = K_{app} \times t \quad (3)$$

$$417 \quad t_{1/2} = \frac{0.693}{K_{app}} \quad (4)$$

418 where **K<sub>app</sub>** (min<sup>-1</sup>) is the apparent degradation rate constant of the first-order reaction, t is the  
 419 irradiation time (min), C<sub>0</sub> (mg/L) and C<sub>t</sub> (mg/L) are the initial and residual concentrations of  
 420 MG dye.

421 The linearization of ln (C<sub>t</sub>/C<sub>0</sub>) as a function of irradiation time for each photocatalyst is given  
 422 in **Figure. 12c**. The calculated values of **K<sub>app</sub>** and half-life **t<sub>1/2</sub>** were also reported in **Table 3**.

423 **Table 2.** Comparison of photocatalytic activity of g-C<sub>3</sub>N<sub>4</sub>/Fe<sub>3</sub>O<sub>4</sub>/Ag<sub>3</sub>PO<sub>4</sub>@Sep towards MG  
 424 dye with other similar photocatalysts from literature.



Photocatalyst	Light Source	C <sub>0</sub> (mg/L)	Time (min)	%	Ref
ZnO/CNT	Visible light	30	60	79 %	[39]
$\alpha$ -NiMoO <sub>4</sub>	UV– Visible	10	180	79.43 %	[40]
poly(azomethine)/Ti O <sub>2</sub>	Sunlight	50	300	95	[41]
rGO/CuS	Sunlight	10	90	97.6%	[42]
Fe <sub>3</sub> O <sub>4</sub> / SiO <sub>2</sub> /TiO <sub>2</sub>	UV	10	150	100%	[43]
Pt-TiO <sub>2</sub> /SiO <sub>2</sub>	UV–Vis. light	10	60	79%	[44]
RGO-Fe <sub>3</sub> O <sub>4</sub> /TiO <sub>2</sub>	UV–Visible	5.5	55	100	[45]
<b>g-C<sub>3</sub>N<sub>4</sub>/Fe<sub>3</sub>O<sub>4</sub>/Ag<sub>3</sub>PO<sub>4</sub>@Sep</b>	<b>Sunlight</b>	<b>10</b>	<b>12</b>	<b>100</b>	<b>This work</b>

425

426 **Table 3.** MG dye degradation parameters for different prepared photocatalysts.

	g-C <sub>3</sub> N <sub>4</sub>	g-C <sub>3</sub> N <sub>4</sub> @Sep	g-C <sub>3</sub> N <sub>4</sub> /Ag <sub>3</sub> PO <sub>4</sub> @Sep	g-C <sub>3</sub> N <sub>4</sub> /Fe <sub>3</sub> O <sub>4</sub> /Ag <sub>3</sub> PO <sub>4</sub> @Sep
<b>K<sub>app</sub> (min<sup>-1</sup>)</b>	0.0097	0.01	0.143	0.264
<b>t<sub>1/2</sub> (min)</b>	4.34	4.238	1.64	0.96

427

428 The obtained rate constants (K<sub>app</sub>) values for the g-C<sub>3</sub>N<sub>4</sub>, g-C<sub>3</sub>N<sub>4</sub>@Sep, g-C<sub>3</sub>N<sub>4</sub>/Ag<sub>3</sub>PO<sub>4</sub>@Sep  
429 and g-C<sub>3</sub>N<sub>4</sub>/Fe<sub>3</sub>O<sub>4</sub>/Ag<sub>3</sub>PO<sub>4</sub>@Sep nanocomposites are, 0.0097, 0.01, 0.143 and 0.26 min<sup>-1</sup>,  
430 respectively. The use of the g-C<sub>3</sub>N<sub>4</sub>/Fe<sub>3</sub>O<sub>4</sub>/Ag<sub>3</sub>PO<sub>4</sub>@Sep nanocomposite indicates  
431 enhancement of the MG dye photocatalytic degradation, under solar irradiation, leading to a  
432 higher rate constant K<sub>app</sub> value, which is 27, 26 and 1.85 times higher than g-C<sub>3</sub>N<sub>4</sub>, g-  
433 C<sub>3</sub>N<sub>4</sub>@Sep, g-C<sub>3</sub>N<sub>4</sub>/Ag<sub>3</sub>PO<sub>4</sub>@Sep, respectively. Therefore, the photocatalytic enhancement of



434 magnetic nanocomposite  $g\text{-C}_3\text{N}_4/\text{Fe}_3\text{O}_4/\text{Ag}_3\text{PO}_4@\text{Sep}$  to degrade organic molecules such as  
 435 MG dye under solar light irradiation was attributed to the synergy effects occurring between  
 436  $\text{Ag}_3\text{PO}_4$  supported by sepiolite clay and  $g\text{-C}_3\text{N}_4$  combined with the  $\text{Fe}_3\text{O}_4$  nanoparticles.

437

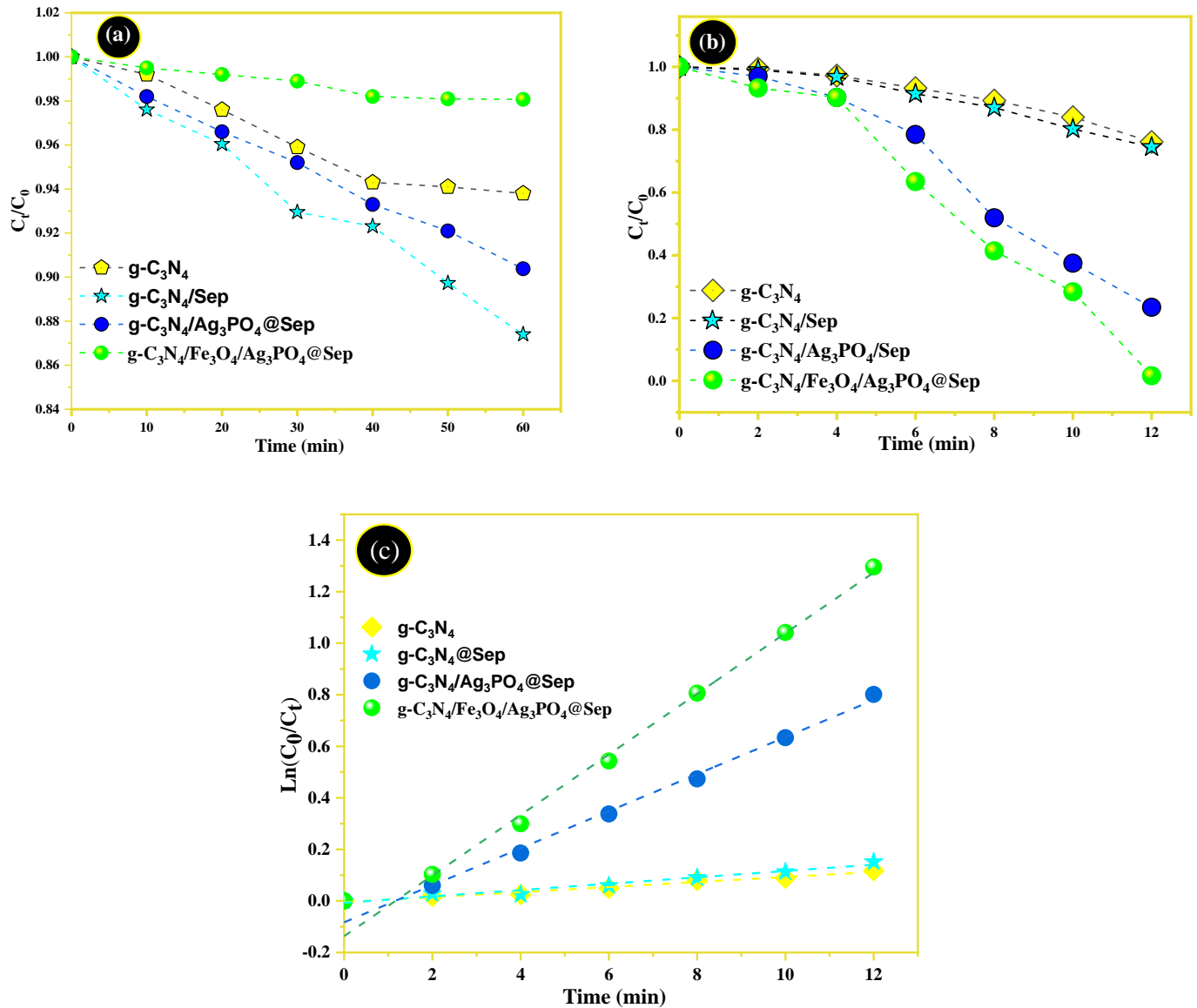


**Figure.12.** Irradiation of MG aqueous solution in the absence of the photocatalyst, and adsorption curves of MG dye from water onto various prepared samples, in the absence of the sunlight irradiation (a). Photocatalytic activities in the presence of various photocatalysts for MG degradation, and under sun light irradiation (b). Pseudo-first-order kinetic plot for degradation of the MG dye (c).

The pH is one of the important factors in the photocatalytic process because it affects the surface charge of the photocatalyst, degree of ionization of the target organic pollutants and dissociation of the functional groups on the active site of the photocatalyst [46]. **Figure.13** displays the influence of initial pH on the photodegradation of malachite green (10 mg. L<sup>-1</sup>) catalyzed by g-C<sub>3</sub>N<sub>4</sub>/Fe<sub>3</sub>O<sub>4</sub>/Ag<sub>3</sub>PO<sub>4</sub>@Sep, which were performed by changing the pH in the range of 3-11 and adjusted by NaOH (0.1 M) or HCl (0.1 M). It is observed that the g-C<sub>3</sub>N<sub>4</sub>/Fe<sub>3</sub>O<sub>4</sub>/Ag<sub>3</sub>PO<sub>4</sub>@Sep nanocomposite exhibits the greatest photocatalytic efficiency at pH = 7 (approximately 100%). However, in the acidic medium is reduced to 65.76% and 83.53% at pH = 3 and pH=5 which can be due to the fact that in acidic media, the surface of Sepiolite can be surrounded by the positive charges of H<sup>+</sup>, which prevents the cationic MG molecules from reaching the active site active site of Ag<sub>3</sub>PO<sub>4</sub> and g-C<sub>3</sub>N<sub>4</sub>. Nevertheless, under a strongly alkaline solution pH =9 and pH =11, the degradation efficiency is decreased to 25.15% and 20.62%. This can be related to the instability of g-C<sub>3</sub>N<sub>4</sub>/Fe<sub>3</sub>O<sub>4</sub>/Ag<sub>3</sub>PO<sub>4</sub>@Sep nanocomposite in a strong alkaline solution (Ag<sub>3</sub>PO<sub>4</sub> can react with NaOH to form Ag<sub>2</sub>O, and then reduces the degradation performance). Hence, pH=7 was found to be more adequate for MG degradation.

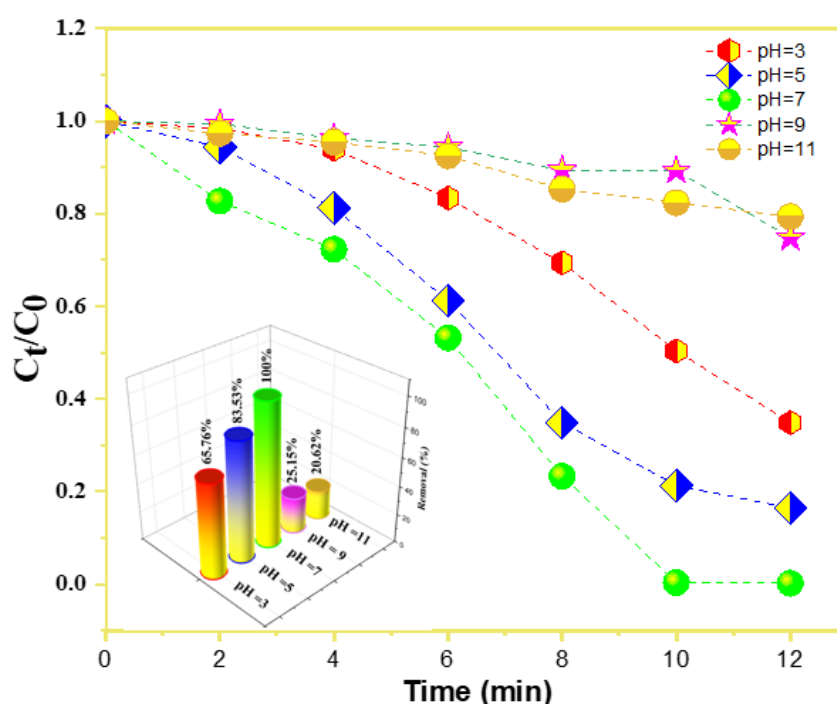


**Figure. 13** Effect of pH values on MG photocatalytic degradation by g-C<sub>3</sub>N<sub>4</sub>/Fe<sub>3</sub>O<sub>4</sub>/Ag<sub>3</sub>PO<sub>4</sub>@Sep

### 439 3.3. Possible photocatalytic mechanism

440 In order further to understand the photocatalytic mechanism of  $g\text{-C}_3\text{N}_4/\text{Fe}_3\text{O}_4/\text{Ag}_3\text{PO}_4@\text{Sep}$   
441 nanocomposites in details. Several active species, like the hydroxyl radical ( $\cdot\text{OH}$ ), the hole  
442 ( $h^+$ ), and the superoxide anion radical ( $\cdot\text{O}_2^-$ ) are participate in the photodegradation processes,  
443 and the function of active species generated by nanocomposite photocatalysts is evaluated  
444 with different scavengers. However, the typical radical trapping tests for MG dye degradation  
445 were examined in the presence of ethylenediamine tetra-acetic acid disodium (EDTA-2Na),  
446 L-ascorbic acid (ASC), and Isopropanol Alcohol (IPA), which are utilized as capture agents  
447 for  $h^+$ ,  $\cdot\text{O}_2^-$ , and  $\cdot\text{OH}$ , respectively [37]. It can be seen from **Figure. 14** that the removal rate  
448 of MG by  $g\text{-C}_3\text{N}_4/\text{Fe}_3\text{O}_4/\text{Ag}_3\text{PO}_4@\text{Sep}$  photocatalyst was achieved up to 100 % under 12  
449 minutes of visible light irradiation, without the introduction of a capture agent. Besides, the  
450 decolorization activity of  $g\text{-C}_3\text{N}_4/\text{Fe}_3\text{O}_4/\text{Ag}_3\text{PO}_4@\text{Sep}$  nanocomposite towards MG dye in the  
451 presence of EDTA-2Na, IPA and ASC decreased to 16.35%, 10.44% and 87.6%, respectively,  
452 indicating that  $\cdot\text{O}_2^-$  was not the main reactive species in the degradation photocatalytic  
453 activity. Whereas the photocatalytic activity was strongly inhibited by the introduction of  
454 EDTA- 2Na and IPA, which indicated that that  $h^+$  and  $\cdot\text{OH}$  are the major reactive species in  
455 the photocatalytic degradation of MG. Therefore,  $h^+$  and  $\cdot\text{OH}$  radical are expected to be the  
456 main reactive species for  $g\text{-C}_3\text{N}_4/\text{Fe}_3\text{O}_4/\text{Ag}_3\text{PO}_4@\text{Sep}$  nanocomposite in the photocatalytic  
457 degradation process of MG under sunlight illumination. While ( $\cdot\text{O}_2^-$ ) played a secondary role.  
458 The same results were obtained in the previous study [13].

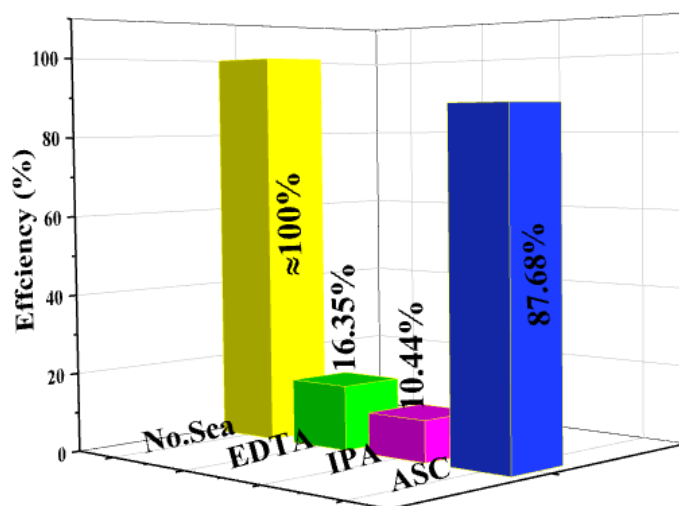


**Figure. 14.** Effect of scavengers on the photocatalytic degradation of MG by  $g\text{-C}_3\text{N}_4/\text{Fe}_3\text{O}_4/\text{Ag}_3\text{PO}_4@\text{Sep}$  nanocomposite.

460 The possible mechanism of the improved photocatalytic activity for g-  
 461 C<sub>3</sub>N<sub>4</sub>/Fe<sub>3</sub>O<sub>4</sub>/Ag<sub>3</sub>PO<sub>4</sub>@Sep toward MG dye was investigated based on our previous  
 462 experimental and schematically illustrated in **Figure. 15**. For two pure Ag<sub>3</sub>PO<sub>4</sub> and g-C<sub>3</sub>N<sub>4</sub>,  
 463 the electrons and holes photogenerated tend to recombine, and then only a proportion of them  
 464 participated in the photocatalytic reaction. Thus, resulting in a comparatively low  
 465 photocatalytic activity. However, the CB and VB positions of Ag<sub>3</sub>PO<sub>4</sub> and g-C<sub>3</sub>N<sub>4</sub> were  
 466 determined using the empirical equations as shown below[46]:

$$467 \quad \chi(A_a B_b C_c) = [\chi(A)^a \cdot \chi(B)^b \cdot \chi(C)^c]^{\frac{1}{a+b+c}} \quad (5)$$

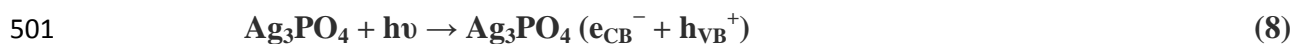
$$468 \quad E_{CB} = \chi - E_0 - \frac{E_g}{2} \quad (6)$$

$$469 \quad E_{VB} = E_{CB} + E_g \quad (7)$$

470 where  $\chi$  indicates the absolute electronegativity of the semiconductor, which is defined as the  
 471 geometric mean of the absolute electronegativity of the constituent atoms,  $E_0$  is the energy of  
 472 free electrons on the hydrogen scale (about 4.5 eV vs. NHE) and  $E_g$  (eV) the band gap energy  
 473 of the semiconductors. The  $\chi$  values for Ag<sub>3</sub>PO<sub>4</sub> and g-C<sub>3</sub>N<sub>4</sub> are calculated to be 5.96 and  
 474 4.73, respectively. The CB and VB positions of g-C<sub>3</sub>N<sub>4</sub> are determined to be -1.24 and +1.7  
 475 eV, respectively, whereas those of Ag<sub>3</sub>PO<sub>4</sub> are about +0.13 and +2.68 V, respectively (**Table**  
 476 **4**). In this study the sepiolite clay was used as a support for the three semiconductors which  
 477 helped to increase the adsorptive properties of the g-C<sub>3</sub>N<sub>4</sub>/Fe<sub>3</sub>O<sub>4</sub>/Ag<sub>3</sub>PO<sub>4</sub>@Sep  
 478 nanocomposite surface, and to enhance its anionic active sites density, leading to removal  
 479 from water of more hazardous MG dye molecules [43].

480 Due to the irradiation of sunlight, the electrons in the valence band (VB) of Ag<sub>3</sub>PO<sub>4</sub> can be  
 481 rapidly transferred from the conduction band (CB) leaving holes (h<sup>+</sup>). Besides, the g-  
 482 C<sub>3</sub>N<sub>4</sub> was also very activated by sunlight photons, and the generate the electrons in the  
 483 conduction band (CB) and holes in the valence band (VB). At the same time, the Fe<sub>3</sub>O<sub>4</sub>  
 484 nanoparticles were used as a solid electron mediator to link Ag<sub>3</sub>PO<sub>4</sub> and g-C<sub>3</sub>N<sub>4</sub> and can it  
 485 enhances the electron transfer capability of photocarriers. On the other hand, the photo-  
 486 generated electrons (e<sup>-</sup>) formed in the CB of Ag<sub>3</sub>PO<sub>4</sub> were captured by the Fe<sub>3</sub>O<sub>4</sub>  
 487 nanoparticles and transferred rapidly to VB of g-C<sub>3</sub>N<sub>4</sub>, because the <sup>•</sup>O<sub>2</sub> radicals cannot be  
 488 formed in the surface of Ag<sub>3</sub>PO<sub>4</sub> due to the CB potential ( E<sub>CB</sub> = 0.24 eV) is more positive  
 489 than that of the O<sub>2</sub>/<sup>•-</sup>O<sub>2</sub> potential (-0.046 V vs NHE)[47]. Nevertheless, g-C<sub>3</sub>N<sub>4</sub> can react with  
 490 O<sub>2</sub> to produce the OH<sup>•</sup> radical species through the reduction of O<sub>2</sub> to H<sub>2</sub>O<sub>2</sub>, followed by the

491 further reduction of H<sub>2</sub>O<sub>2</sub> to OH<sup>-</sup> and the OH<sup>•</sup> radical species. This is due to the CB edge  
 492 potential of g-C<sub>3</sub>N<sub>4</sub> (E<sub>CB</sub> = - 1.24 eV / NHE) being more lower than the standard potential of  
 493 the O<sub>2</sub>/H<sub>2</sub>O<sub>2</sub> redox couple, which is 0.68 eV at the normal hydrogen electrode (NHE).  
 494 Consequently, the accumulation of electrons in the CB of g-C<sub>3</sub>N<sub>4</sub> and the holes in the VB of  
 495 Ag<sub>3</sub>PO<sub>4</sub> exhibited a high reduction and oxidation ability to mineralize MG dyes in H<sub>2</sub>O and  
 496 CO<sub>2</sub>, respectively. In the above results, it is clear that the fabricated nanocomposite act as a  
 497 Z-scheme photocatalysts and the synergistic effect between three synthesized semiconductor  
 498 play a curcial role in the enhanced photoctalytic efficiency. Consequently, the  
 499 photodegradation activity of g-C<sub>3</sub>N<sub>4</sub>/Fe<sub>3</sub>O<sub>4</sub>/Ag<sub>3</sub>PO<sub>4</sub>@Sep toward MG dye could be displayed  
 500 as follows:



507

508 **Table 4.** Values of the electronegativity ( $\chi$ ), the bang gap energy (E<sub>g</sub>), and the potential  
 509 energy for valence band (E<sub>VB</sub>) and conduction band (E<sub>CB</sub>), for the g-C<sub>3</sub>N<sub>4</sub> and  
 510 Ag<sub>3</sub>PO<sub>4</sub> catalysts.

catalyst	$\chi$	E <sub>g</sub> (eV)	CB (eV)	VB (eV)
g-C <sub>3</sub> N <sub>4</sub>	4.73	2.94	-1.24	1.7
Ag <sub>3</sub> PO <sub>4</sub>	5.96	2.44	0,24	2,68

511

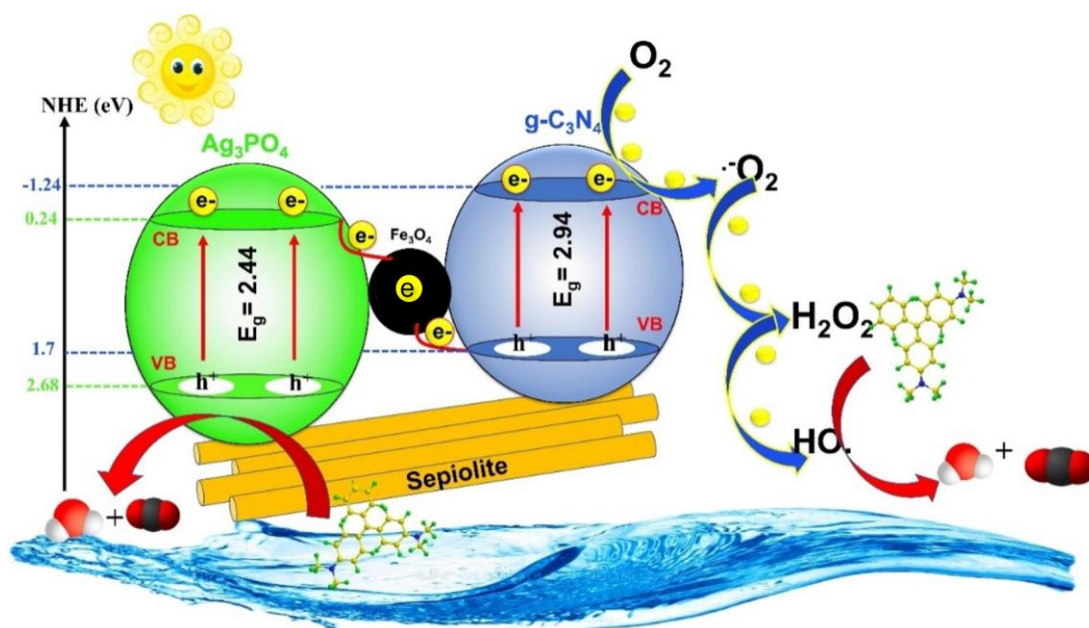


**Figure. 15** : Schematic Illustration of Photocatalytic activity toward MG dye using  $g\text{-C}_3\text{N}_4/\text{Fe}_3\text{O}_4/\text{Ag}_3\text{PO}_4@\text{Sep}$  nanocomposite under sun-Light Irradiation.

512

### 513 3.4. Reusability and stability

514 The stability of photocatalysts is also an essential characteristic from the point of view of  
 515 practical applications[49]. To investigated stability and the reusability of the  $g\text{-C}_3\text{N}_4/\text{Fe}_3\text{O}_4/\text{Ag}_3\text{PO}_4@\text{Sep}$   
 516 and  $\text{Ag}_3\text{PO}_4$  samples, the recycle experiments for the degradation  
 517 of MG dye under sunlight illumination in 12 min was studied. As illustrated in **Figure. 16**,  
 518 after four cycles, the degradation of MG dye by pure  $\text{Ag}_3\text{PO}_4$  exhibited an evident decrease  
 519 (<22%) due to their high solubility in aqueous solution and the photoreduction of  $\text{Ag}^+$  in  
 520  $\text{Ag}_3\text{PO}_4$  to metallic Ag under sunlight illumination ( $4\text{Ag}_3\text{PO}_4 + 6\text{H}_2\text{O} + 12\text{h}^+ + 12\text{e}^- \rightarrow 12\text{Ag} +$   
 521  $4\text{H}_3\text{PO}_4 + 3\text{O}_2$ ). Also, part of the pure  $\text{Ag}_3\text{PO}_4$  may degrade to  $\text{Ag}_2\text{O}$  when  $\text{Ag}_3\text{PO}_4$  is used. In  
 522 the other hand (<13%), the photocatalytic activity of  $g\text{-C}_3\text{N}_4/\text{Fe}_3\text{O}_4/\text{Ag}_3\text{PO}_4@\text{Sep}$   
 523 nanocomposite shows a small loss, suggesting that the nanocomposite photocatalyst is  
 524 comparatively stable during the photocatalytic degradation of MG dyes, which might be due  
 525 to the fact that  $g\text{-C}_3\text{N}_4$ ,  $\text{Fe}_3\text{O}_4$  and sepiolite prevented  $\text{Ag}_3\text{PO}_4$  from being reduced to metallic  
 526 silver under sunlight irradiation. However, the color of the  $g\text{-C}_3\text{N}_4/\text{Fe}_3\text{O}_4/\text{Ag}_3\text{PO}_4@\text{Sep}$   
 527 nanocomposite slightly changed, while the pure  $\text{Ag}_3\text{PO}_4$  changed to gray. We hypothesized  
 528 that the photocorrosion phenomenon happened in the pure  $\text{Ag}_3\text{PO}_4$  nanoparticles. Thus, the  
 529 enhanced photostability of  $g\text{-C}_3\text{N}_4/\text{Fe}_3\text{O}_4/\text{Ag}_3\text{PO}_4@\text{Sep}$  had the potential for long-term  
 530 wastewater purification.

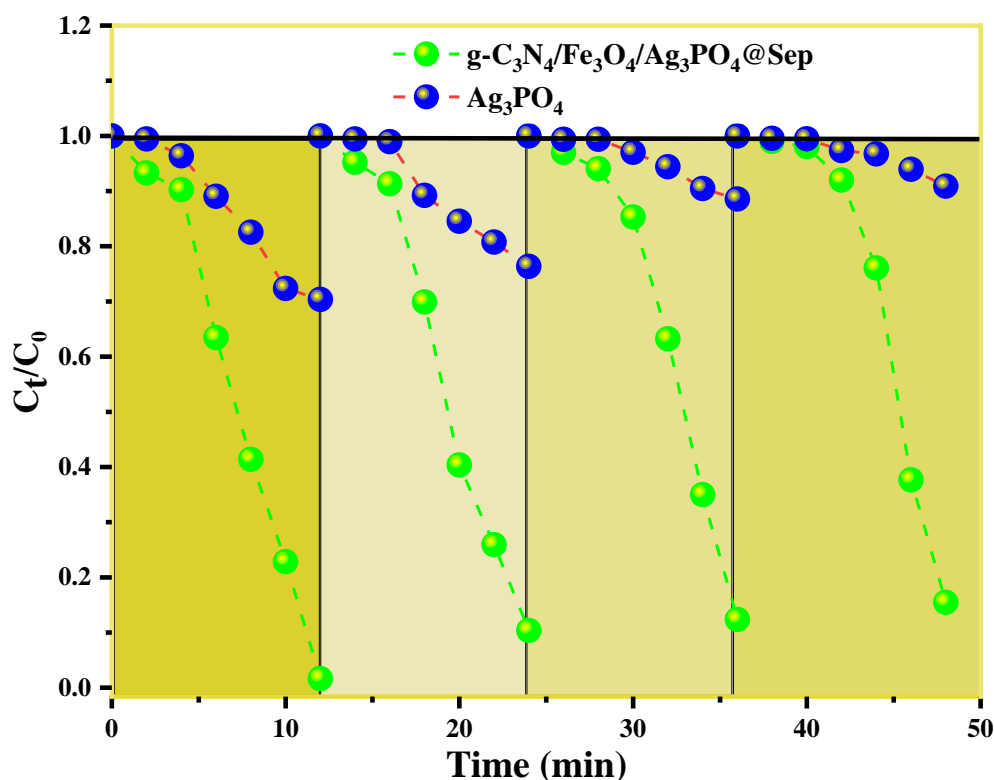


**Figure. 16.** Cycling runs for photocatalytic degradation of MG dye using g-C<sub>3</sub>N<sub>4</sub>/Fe<sub>3</sub>O<sub>4</sub>/Ag<sub>3</sub>PO<sub>4</sub>@Sep and Ag<sub>3</sub>PO<sub>4</sub> under sunlight irradiation.

531

### 532 **3.5. The formation of nano-composite Fe<sub>3</sub>O<sub>4</sub>/Ag<sub>3</sub>PO<sub>4</sub>@Sep by Monte Carlo adsorption** 533 **locator simulation**

534 After optimization of structures by quantum calculations based on DFT-D, the adsorption  
 535 performance of 6 of g-C<sub>3</sub>N<sub>4</sub>, Ag<sub>3</sub>PO<sub>4</sub> and Fe<sub>3</sub>O<sub>4</sub> molecules on Sep was occurred to make  
 536 Fe<sub>3</sub>O<sub>4</sub>/Ag<sub>3</sub>PO<sub>4</sub>@Sep surface by adsorption locator module and forcefield; universal in  
 537 Materials Studio 2017 software (ball-and-stick structures of nanocomposite are in **Figures**  
 538 **17a-b**. The total energy of the system after the adsorption of C<sub>3</sub>N<sub>4</sub>, Ag<sub>3</sub>PO<sub>4</sub> and Fe<sub>3</sub>O<sub>4</sub> (E<sub>ad</sub>) on  
 539 Sep was obtained about  $-4.984 \times 10^3$  kcal/mol, resulting in coadsorbed g-C<sub>3</sub>N<sub>4</sub>, Ag<sub>3</sub>PO<sub>4</sub> and  
 540 Fe<sub>3</sub>O<sub>4</sub> owing to the high negative value and exothermic system. In other hand, the calculated  
 541 adsorption energy of this configuration was the most stable. Additionally, the top view of the  
 542 Fe<sub>3</sub>O<sub>4</sub> molecule vertically adsorbed on Sep are shown in **Figure.2b**. The energy of rigid  
 543 adsorption, deformation, E<sub>ads</sub> of Ag<sub>3</sub>PO<sub>4</sub>, Fe<sub>3</sub>O<sub>4</sub> and C<sub>3</sub>N<sub>4</sub> was obtained -439.766,  $-4.544 \times 10^3$ ,  
 544 -11.147, -478.748 and -335.253, respectively. By analysis and comparison, adsorption energy  
 545 for Fe<sub>3</sub>O<sub>4</sub> and g-C<sub>3</sub>N<sub>4</sub> parallel to Sep and their adsorption energies of both configurations were  
 546 higher than that of Ag<sub>3</sub>PO<sub>4</sub>.



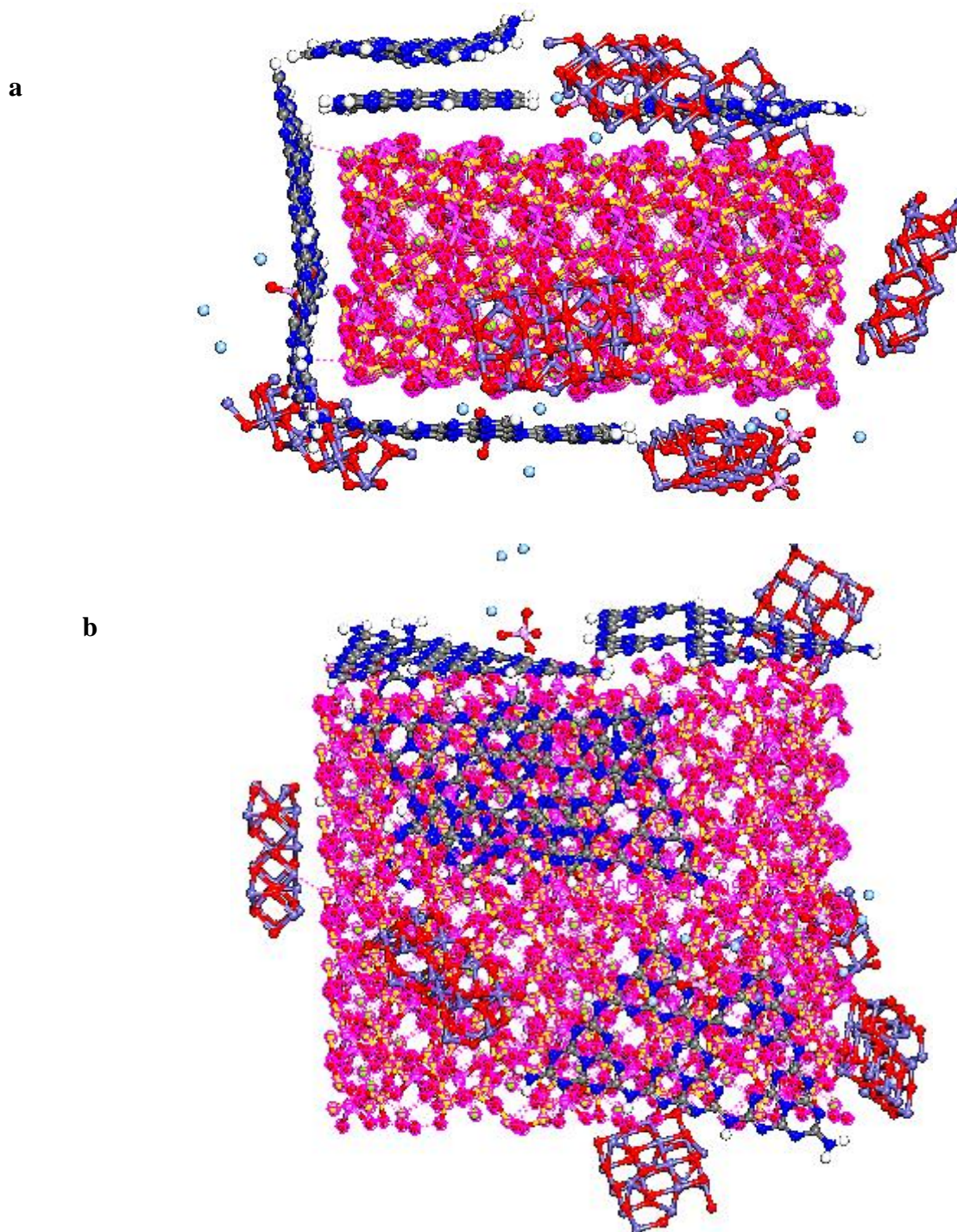


**Figure. 17.** (a and b); side and top views of the adsorption of 6  $C_3N_4$ ,  $Ag_3PO_4$  and  $Fe_3O_4$  molecules on Sep by adsorption locator module in Materials Studio 2017 software.

547

548 **3.6. MG adsorption on  $Fe_3O_4/Ag_3PO_4@Sep$  by Monte Carlo adsorption locator**  
 549 **simulation**

550 In order to determine the most favorable adsorption geometry of MG on  $Fe_3O_4/Ag_3PO_4@Sep$ ,  
 551 6 MG molecules were applied to adsorb on nano-composite in the gas phase by adsorption



552 locator module and forcefield; universal in Materials Studio 2017 software (**Figures 18a-b**).  
553 The total energy of the system after the adsorption of MG ( $E_{ad}$ ) on adsorbent was estimated  
554 about -436.229 kcal/mol as non-covalent interactions. The above adsorption energy reflected  
555 the thermodynamic stability of the whole adsorption system due to the negative value[50]. In  
556 other hand, the interaction was spontaneous and exothermic[51]. Based on the adsorption  
557 results, MG can be transported horizontally by van der Waals and electrostatic interactions as  
558 well as  $\pi$ - $\pi$  stack between  $C_3N_4$  and the delocalized  $\pi$  electron of MG, resulting dye  
559 elimination. The significant adsorption of the MG can be related  $\pi$ - $\pi$  stack interactions by g-  
560  $C_3N_4$ [52]. The computational studies revealed that all MG molecules on nanocomposite were  
561 the physisorption[53].

562

563

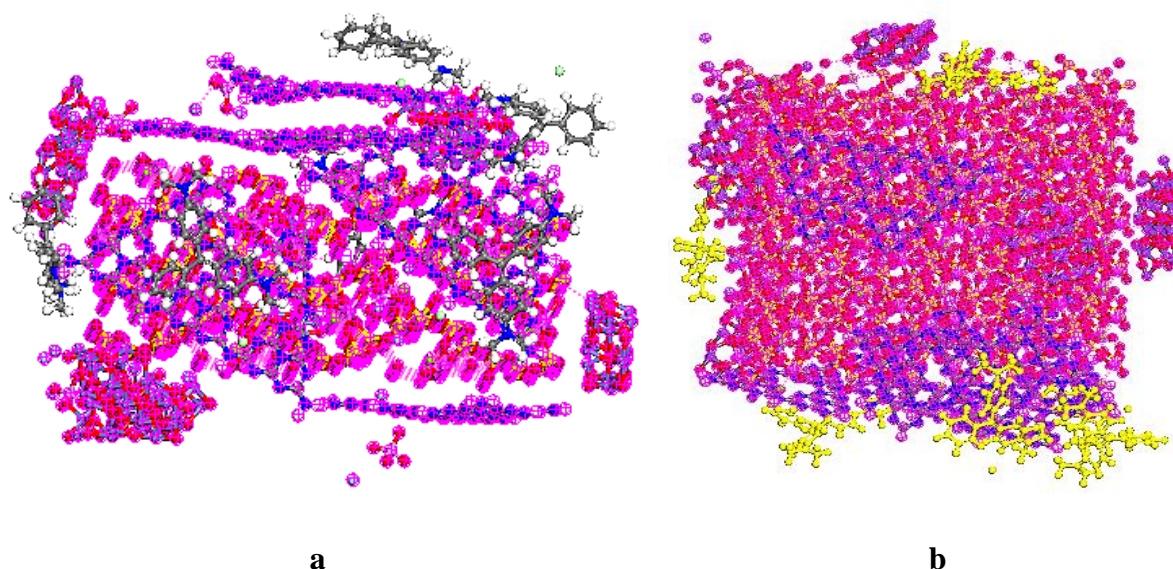


**Figure. 18.** (a and b); views of the adsorption of 6 MG molecules on  $Fe_3O_4/Ag_3PO_4@Sep$  by adsorption locator module in Materials Studio 2017 software.

564

## 565 **Conclusion**

566 In brief, a simple approach synthesis was used to produce  $g-C_3N_4/Fe_3O_4/Ag_3PO_4@Sep$   
567 photocatalysts. The sepiolite clay was used as a support for the three semiconductors  
568 investigated  $Ag_3PO_4$ ,  $g-C_3N_4$  and  $Fe_3O_4$ . Based on the characterization results,  $Ag_3PO_4$ ,  $g$ -  
569  $C_3N_4$  and  $Fe_3O_4$  particles were formed on the sepiolite clay surface with intimate interactions  
570 occurring between them. The  $g-C_3N_4/Fe_3O_4/Ag_3PO_4@Sep$  magnetic nanocomposite in

571 comparison to the others prepared photocatalysts, was found to be the most stable and it  
572 showed the higher activities for the MG degradation under sunlight irradiation. The  
573 photocatalytic enhancement of magnetic nanocomposite g-C<sub>3</sub>N<sub>4</sub>/Fe<sub>3</sub>O<sub>4</sub>/Ag<sub>3</sub>PO<sub>4</sub>@Sep to  
574 degrade organic molecules such as MG dye under solar light irradiation was attributed to the  
575 synergy effects occurring between the Ag<sub>3</sub>PO<sub>4</sub>, the g-C<sub>3</sub>N<sub>4</sub> and the Fe<sub>3</sub>O<sub>4</sub> nanoparticles,  
576 supported by the. sepiolite clay. The overall data indicate that the co-precipitation method,  
577 presented in this work, is a suitable approach to design and to synthesis new magnetic Z-  
578 scheme nanocomposite photocatalysts with enhanced stability and activity towards MG  
579 degradation. At the first, all structures were optimized by DFT-D in Material Studio 2017.  
580 The next stage, adsorption locator module was applied to adsorb Fe<sub>3</sub>O<sub>4</sub> and Ag<sub>3</sub>PO<sub>4</sub> on Sep,  
581 resulting exothermic system due to the high negative energy. Then, the adsorption mechanism  
582 of MG onto Fe<sub>3</sub>O<sub>4</sub>/Ag<sub>3</sub>PO<sub>4</sub>@Sep nano-composite was computationally investigated using MD  
583 through adsorption locator module. The result showed that MG was adsorbed through  
584 physisorption into nano-composit by using van der Waals and electrostatic interactions as  
585 well as  $\pi$ - $\pi$  stack between C<sub>3</sub>N<sub>4</sub> and MG. by MG adsorption, MG degradation can be  
586 happened by nanocomposite. This DFT simulation result confirmed experimental results.

## 587 **Reference**

- 588 1. Ouachtak, H., Akhouairi, S., Haounati, R., Addi, A.A., Jada, A., Taha, M.L., Douch, J.:  
589 3,4-dihydroxybenzoic acid removal from water by goethite modified natural sand  
590 column fixed-bed: Experimental study and mathematical modeling. *Desalin. Water*  
591 *Treat.* 194, 439–449 (2020). <https://doi.org/10.5004/dwt.2020.25562>
- 592 2. Inyinbor, A.A., Bello, O.S., Fadiji, A.E., Inyinbor, H.E.: Threats from antibiotics: A  
593 serious environmental concern. *J. Environ. Chem. Eng.* 6, 784–793 (2018).  
594 <https://doi.org/10.1016/j.jece.2017.12.056>
- 595 3. Cheng, D., Ngo, H.H., Guo, W., Lee, D., Nghiem, D.L., Zhang, J., Liang, S., Varjani,  
596 S., Wang, J.: Performance of microbial fuel cell for treating swine wastewater  
597 containing sulfonamide antibiotics. *Bioresour. Technol.* 311, 123588 (2020).  
598 <https://doi.org/10.1016/j.biortech.2020.123588>
- 599 4. Schwarzenbach, R.P., Egli, T., Hofstetter, T.B., von Gunten, U., Wehrli, B.: Global  
600 Water Pollution and Human Health. *Annu. Rev. Environ. Resour.* 35, 109–136 (2010).  
601 <https://doi.org/10.1146/annurev-environ-100809-125342>

- 602 5. Samanta, P., Desai, A. V., Let, S., Ghosh, S.K.: Advanced Porous Materials for  
603 Sensing, Capture and Detoxification of Organic Pollutants toward Water Remediation.  
604 ACS Sustain. Chem. Eng. 7, 7456–7478 (2019).  
605 <https://doi.org/10.1021/acssuschemeng.9b00155>
- 606 6. Huang, Q., Song, S., Chen, Z., Hu, B., Chen, J., Wang, X.: Biochar-based materials and  
607 their applications in removal of organic contaminants from wastewater: state-of-the-art  
608 review. Biochar. 1, 45–73 (2019). <https://doi.org/10.1007/s42773-019-00006-5>
- 609 7. Nithya, R., Thirunavukkarasu, A., Sathya, A.B., Sivashankar, R.: Magnetic materials  
610 and magnetic separation of dyes from aqueous solutions: a review. Environ. Chem.  
611 Lett. 19, 1275–1294 (2021). <https://doi.org/10.1007/s10311-020-01149-9>
- 612 8. Largo, F., Haounati, R., Akhouairi, S., Ouachtak, H., El Haouti, R., El Guerdaoui, A.,  
613 Hafid, N., Santos, D.M.F., Akbal, F., Kuleyin, A., Jada, A., Addi, A.A.: Adsorptive  
614 removal of both cationic and anionic dyes by using sepiolite clay mineral as adsorbent:  
615 Experimental and molecular dynamic simulation studies. J. Mol. Liq. 318, 114247  
616 (2020). <https://doi.org/10.1016/j.molliq.2020.114247>
- 617 9. Haounati, R., Ouachtak, H., El Haouti, R., Akhouairi, S., Largo, F., Akbal, F.,  
618 Benlhachemi, A., Jada, A., Addi, A.A.: Elaboration and properties of a new  
619 SDS/CTAB@Montmorillonite organoclay composite as a superb adsorbent for the  
620 removal of malachite green from aqueous solutions. Sep. Purif. Technol. 255, 117335  
621 (2021). <https://doi.org/10.1016/j.seppur.2020.117335>
- 622 10. Yang, H., Yan, Z., Du, X., Bai, L., Yu, H., Ding, A., Li, G., Liang, H., Aminabhavi,  
623 T.M.: Removal of manganese from groundwater in the ripened sand filtration:  
624 Biological oxidation versus chemical auto-catalytic oxidation. Chem. Eng. J. 382,  
625 123033 (2020). <https://doi.org/10.1016/j.cej.2019.123033>
- 626 11. Bouddouch, A., Amaterz, E., Bakiz, B., Taoufyq, A., Guinneton, F., Villain, S.,  
627 Gavarrì, J.R., Ezahri, M., Valmalette, J.C., Benlhachemi, A.: Role of thermal  
628 decomposition process in the photocatalytic or photoluminescence properties of BiPO<sub>4</sub>  
629 polymorphs. Water Environ. Res. 1–14 (2020). <https://doi.org/10.1002/wer.1340>
- 630 12. Amaterz, E., Tara, A., Bouddouch, A., Taoufyq, A., Bakiz, B., Benlhachemi, A., Jbara,  
631 O.: Photo-electrochemical degradation of wastewaters containing organics catalysed by  
632 phosphate-based materials: a review. Rev. Environ. Sci. Biotechnol. 9, (2020).

- 633 <https://doi.org/10.1007/s11157-020-09547-9>
- 634 13. Haounati, R., El Guerdaoui, A., Ouachtak, H., El Haouti, R., Bouddouch, A., Hafid, N.,  
635 Bakiz, B., Santos, D.M.F., Labd Taha, M., Jada, A., Ait Addi, A.: Design of direct Z-  
636 scheme superb magnetic nanocomposite photocatalyst Fe<sub>3</sub>O<sub>4</sub>/Ag<sub>3</sub>PO<sub>4</sub>@Sep for  
637 hazardous dye degradation. *Sep. Purif. Technol.* 277, 119399 (2021).  
638 <https://doi.org/10.1016/j.seppur.2021.119399>
- 639 14. Natarajan, S., Bajaj, H.C., Tayade, R.J.: Recent advances based on the synergetic effect  
640 of adsorption for removal of dyes from waste water using photocatalytic process. *J.*  
641 *Environ. Sci.* 65, 201–222 (2018)
- 642 15. Cai, T., Zeng, W., Liu, Y., Wang, L., Dong, W., Chen, H., Xia, X.: A promising  
643 inorganic-organic Z-scheme photocatalyst Ag<sub>3</sub>PO<sub>4</sub>/PDI supermolecule with enhanced  
644 photoactivity and photostability for environmental remediation. *Appl. Catal. B*  
645 *Environ.* 263, 118327 (2020). <https://doi.org/10.1016/j.apcatb.2019.118327>
- 646 16. Sulaeman, U., Suhendar, S., Diastuti, H., Riapanitra, A., Yin, S.: Design of Ag<sub>3</sub>PO<sub>4</sub>  
647 for highly enhanced photocatalyst using hydroxyapatite as a source of phosphate ion.  
648 *Solid State Sci.* 86, 1–5 (2018)
- 649 17. Park, H., Son, N., Park, B.H., Liu, C., Joo, S.W., Kang, M.: Switching of a type I to an  
650 all-solid-state Z-scheme heterojunction by an electron mediator rGO bridge: 18.4%  
651 solar-to-hydrogen efficiency in n-ZnS/rGO/p-Bi<sub>2</sub>S<sub>3</sub> ternary catalyst. *Chem. Eng. J.*  
652 430, 133104 (2022). <https://doi.org/10.1016/j.cej.2021.133104>
- 653 18. Iqbal, W., Qiu, B., Lei, J., Wang, L., Zhang, J., Anpo, M.: One-step large-scale highly  
654 active g-C<sub>3</sub>N<sub>4</sub> nanosheets for efficient sunlight-driven photocatalytic hydrogen  
655 production. *Dalt. Trans.* 46, 10678–10684 (2017). <https://doi.org/10.1039/c7dt00849j>
- 656 19. Paquin, F., Rivnay, J., Salleo, A., Stingelin, N., Silva, C.: Multi-phase semicrystalline  
657 microstructures drive exciton dissociation in neat plastic semiconductors. *J. Mater.*  
658 *Chem. C.* 3, 10715–10722 (2015). <https://doi.org/10.1039/b000000x>
- 659 20. Largo, F., Haounati, R., Akhouairi, S., Ouachtak, H., El Haouti, R., El Guerdaoui, A.,  
660 Hafid, N., Santos, D.M.F., Akbal, F., Kuleyin, A., Jada, A., Addi, A.A.: Adsorptive  
661 removal of both cationic and anionic dyes by using sepiolite clay mineral as adsorbent:  
662 Experimental and molecular dynamic simulation studies. *J. Mol. Liq.* 318, (2020).  
663 <https://doi.org/10.1016/j.molliq.2020.114247>

- 664 21. Alvarado, M., Chianelli, R.C., Arrowood, R.M.: Computational Study of the Structure  
665 of a Sepiolite/Thioindigo Mayan Pigment. *Bioinorg. Chem. Appl.* 2012, 1–6 (2012).  
666 <https://doi.org/10.1155/2012/672562>
- 667 22. Feng, L., Liu, J., Abu-Hamdeh, N.H., Bezzina, S., Eshaghi Malekshah, R.: Molecular  
668 dynamics and quantum simulation of different cationic dyes removal from  
669 contaminated water using UiO-66 (Zr)-(COOH)<sub>2</sub> metal–organic framework. *J. Mol.*  
670 *Liq.* 349, 118085 (2022). <https://doi.org/10.1016/j.molliq.2021.118085>
- 671 23. Heidari, Z., Pelalak, R., Malekshah, R.E., Pishnamazi, M., Marjani, A., Sarkar, S.M.,  
672 Shirazian, S.: Molecular modeling investigation on mechanism of cationic dyes  
673 removal from aqueous solutions by mesoporous materials. *J. Mol. Liq.* 329, 115485  
674 (2021). <https://doi.org/10.1016/j.molliq.2021.115485>
- 675 24. Jiang, F., Yan, T., Chen, H., Sun, A., Xu, C., Wang, X.: A g-C<sub>3</sub>N<sub>4</sub>-CdS composite  
676 catalyst with high visible-light-driven catalytic activity and photostability for  
677 methylene blue degradation. *Appl. Surf. Sci.* 295, 164–172 (2014).  
678 <https://doi.org/10.1016/j.apsusc.2014.01.022>
- 679 25. Yan, S.C., Li, Z.S., Zou, Z.G.: Photodegradation performance of g-C<sub>3</sub>N<sub>4</sub> fabricated by  
680 directly heating melamine. *Langmuir.* 25, 10397–10401 (2009).  
681 <https://doi.org/10.1021/la900923z>
- 682 26. Dong, F., Zhao, Z., Xiong, T., Ni, Z., Zhang, W., Sun, Y., Ho, W.: In Situ Construction  
683 of g-C<sub>3</sub>N<sub>4</sub> / g-C<sub>3</sub>N<sub>4</sub> Metal-Free Heterojunction for Enhanced Visible Light  
684 Photocatalysis. (2013)
- 685 27. Zhu, Q., Zhang, Y., Lv, F., Chu, P.K., Ye, Z., Zhou, F.: Cuprous oxide created on  
686 sepiolite: Preparation, characterization, and photocatalytic activity in treatment of red  
687 water from 2,4,6-trinitrotoluene manufacturing. *J. Hazard. Mater.* 217–218, 11–18  
688 (2012). <https://doi.org/10.1016/j.jhazmat.2011.12.053>
- 689 28. Zhang, Y., Wang, D., Zhang, G.: Photocatalytic degradation of organic contaminants  
690 by TiO<sub>2</sub>/sepiolite composites prepared at low temperature. *Chem. Eng. J.* 173, 1–10  
691 (2011). <https://doi.org/10.1016/j.cej.2010.11.028>
- 692 29. Ahadpour Shal, A., Jafari, A.: Study of structural and magnetic properties of  
693 superparamagnetic Fe<sub>3</sub>O<sub>4</sub>-ZnO core-shell nanoparticles. *J. Supercond. Nov. Magn.*  
694 27, 1531–1538 (2014). <https://doi.org/10.1007/s10948-013-2469-9>

- 695 30. Tan, L., Xu, J., Zhang, X., Hang, Z., Jia, Y., Wang, S.: Synthesis of g-C<sub>3</sub>N<sub>4</sub>/CeO<sub>2</sub>  
696 nanocomposites with improved catalytic activity on the thermal decomposition of  
697 ammonium perchlorate. *Appl. Surf. Sci.* 356, 447–453 (2015).  
698 <https://doi.org/10.1016/j.apsusc.2015.08.078>
- 699 31. Xu, H., Zhang, T., Gu, Y., Yan, X., Lu, N., Liu, H., Xu, Z., Xing, Y., Song, Y., Zhang,  
700 Z., Yang, M.: An electrochemical thrombin aptasensor based on the use of graphite-  
701 like C<sub>3</sub>N<sub>4</sub> modified with silver nanoparticles. *Microchim. Acta.* 187, (2020).  
702 <https://doi.org/10.1007/s00604-020-4111-4>
- 703 32. Yang, L., Liu, X., Liu, Z., Wang, C., Liu, G., Li, Q., Feng, X.: Enhanced photocatalytic  
704 activity of g-C<sub>3</sub>N<sub>4</sub> 2D nanosheets through thermal exfoliation using dicyandiamide as  
705 precursor. *Ceram. Int.* 44, 20613–20619 (2018).  
706 <https://doi.org/10.1016/j.ceramint.2018.06.105>
- 707 33. Xu, M., Han, L., Dong, S.: Facile fabrication of highly efficient g-C<sub>3</sub>N<sub>4</sub>/Ag<sub>2</sub>O  
708 heterostructured photocatalysts with enhanced visible-light photocatalytic activity.  
709 *ACS Appl. Mater. Interfaces.* 5, 12533–12540 (2013).  
710 <https://doi.org/10.1021/am4038307>
- 711 34. Zhu, P., Hu, M., Duan, M., Xie, L., Zhao, M.: High visible light response Z-scheme  
712 Ag<sub>3</sub>PO<sub>4</sub> / g-C<sub>3</sub>N<sub>4</sub> / ZnO composite photocatalyst for efficient degradation of  
713 tetracycline hydrochloride: Preparation, properties and mechanism. *J. Alloys Compd.*  
714 840, 155714 (2020). <https://doi.org/10.1016/j.jallcom.2020.155714>
- 715 35. Yan, J., Song, Z., Wang, X., Xu, Y., Pu, W., Xu, H., Yuan, S., Li, H.: Enhanced  
716 photocatalytic activity of ternary Ag<sub>3</sub>PO<sub>4</sub>/GO/g-C<sub>3</sub>N<sub>4</sub> photocatalysts for  
717 Rhodamine B degradation under visible light radiation. *Appl. Surf. Sci.* 466, 70–77  
718 (2019). <https://doi.org/10.1016/j.apsusc.2018.09.234>
- 719 36. Tomke, P.D., Rathod, V.K.: Facile fabrication of silver on magnetic nanocomposite  
720 (Fe<sub>3</sub>O<sub>4</sub>@Chitosan –AgNP nanocomposite) for catalytic reduction of anthropogenic  
721 pollutant and agricultural pathogens. *Int. J. Biol. Macromol.* 149, 989–999 (2020).  
722 <https://doi.org/10.1016/j.ijbiomac.2020.01.183>
- 723 37. Haounati, R., Alakhras, F., Ouachtak, H., Saleh, T.A., Al-Mazaideh, G., Alhajri, E.,  
724 Jada, A., Hafid, N., Addi, A.A.: Synthesized of Zeolite@Ag<sub>2</sub>O Nanocomposite as  
725 Superb Stability Photocatalysis Toward Hazardous Rhodamine B Dye from Water.

- 726 Arab. J. Sci. Eng. (2022). <https://doi.org/10.1007/s13369-022-06899-y>
- 727 38. Schuhl, Y., Baussart, H., Delobel, R., Le Bras, M., Leroy, J.M., Gengembre, L.,  
728 Grimblot, J.: Study of mixed-oxide catalysts containing bismuth, vanadium and  
729 antimony. Preparation, phase composition, spectroscopic characterization and catalytic  
730 oxidation of propene. *J. Chem. Soc. Faraday Trans. 1 Phys. Chem. Condens. Phases.*  
731 *79*, 2055–2069 (1983). <https://doi.org/10.1039/F19837902055>
- 732 39. Arsalani, N., Bazazi, S., Abuali, M., Jodeyri, S.: A new method for preparing  
733 ZnO/CNT nanocomposites with enhanced photocatalytic degradation of malachite  
734 green under visible light. *J. Photochem. Photobiol. A Chem.* *389*, 112207 (2020).  
735 <https://doi.org/10.1016/j.jphotochem.2019.112207>
- 736 40. Palareti, G., Legnani, C., Cosmi, B., Antonucci, E., Erba, N., Poli, D., Testa, S.,  
737 Tosetto, A.: Comparison between different D-Dimer cutoff values to assess the  
738 individual risk of recurrent venous thromboembolism: Analysis of results obtained in  
739 the DULCIS study. *Int. J. Lab. Hematol.* *38*, 42–49 (2016).  
740 <https://doi.org/10.1111/ijlh.12426>
- 741 41. Pradeeba, S.J., Sampath, K., Ramadevi, A.: Photo-catalytic degradations of methylene  
742 blue, malachite green and Bismarck brown using poly(azomethine)/TiO<sub>2</sub>  
743 nanocomposite. *Cluster Comput.* *22*, 3893–3909 (2019).  
744 <https://doi.org/10.1007/s10586-018-2505-4>
- 745 42. El-Hout, S.I., El-Sheikh, S.M., Gaber, A., Shawky, A., Ahmed, A.I.: Highly efficient  
746 sunlight-driven photocatalytic degradation of malachite green dye over reduced  
747 graphene oxide-supported CuS nanoparticles. *J. Alloys Compd.* *849*, 156573 (2020).  
748 <https://doi.org/10.1016/j.jallcom.2020.156573>
- 749 43. Farhadian, M., Kazemzad, M.: Photocatalytic Degradation of Malachite Green by  
750 Magnetic Photocatalyst. *Synth. React. Inorganic, Met. Nano-Metal Chem.* *46*, 458–463  
751 (2016). <https://doi.org/10.1080/15533174.2014.988802>
- 752 44. Afshar, S., Samari Jahromi, H., Jafari, N., Ahmadi, Z., Hakamizadeh, M.: Degradation  
753 of malachite green oxalate by UV and visible lights irradiation using Pt/TiO<sub>2</sub>/SiO<sub>2</sub>  
754 nanophotocatalyst. *Sci. Iran.* *18*, 772–779 (2011).  
755 <https://doi.org/10.1016/j.scient.2011.06.007>
- 756 45. Jaiswal, A., Chattopadhyaya, M.C.: Removal of zinc ion from industrial effluents by

- 757 hydrotalcite-like compound. *Desalin. Water Treat.* 12, 127–132 (2009).  
758 <https://doi.org/10.5004/dwt.2009.943>
- 759 46. Manikandan, V.S., Harish, S., Archana, J., Navaneethan, M.: Fabrication of novel  
760 hybrid Z-Scheme WO<sub>3</sub>@g-C<sub>3</sub>N<sub>4</sub>@MWCNT nanostructure for photocatalytic  
761 degradation of tetracycline and the evaluation of antimicrobial activity. *Chemosphere.*  
762 287, 132050 (2022). <https://doi.org/10.1016/j.chemosphere.2021.132050>
- 763 47. Zhou, Y., Zhang, Y., Lin, M., Long, J., Zhang, Z., Lin, H., Wu, J.C.S., Wang, X.:  
764 Monolayered Bi<sub>2</sub>WO<sub>6</sub> nanosheets mimicking heterojunction interface with open  
765 surfaces for photocatalysis. *Nat. Commun.* 6, 1–8 (2015).  
766 <https://doi.org/10.1038/ncomms9340>
- 767 48. Song, H., Li, Y., Lou, Z., Xiao, M., Hu, L., Ye, Z., Zhu, L.: Synthesis of Fe-doped  
768 WO<sub>3</sub> nanostructures with high visible-light-driven photocatalytic activities. *Appl.*  
769 *Catal. B Environ.* 166–167, 112–120 (2015).  
770 <https://doi.org/10.1016/j.apcatb.2014.11.020>
- 771 49. Wang, W.S., Du, H., Wang, R.X., Wen, T., Xu, A.W.: Heterostructured  
772 Ag<sub>3</sub>PO<sub>4</sub>/AgBr/Ag plasmonic photocatalyst with enhanced photocatalytic activity and  
773 stability under visible light. *Nanoscale.* 5, 3315–3321 (2013).  
774 <https://doi.org/10.1039/c3nr00191a>
- 775 50. Zhu, B., Zhang, L., Xu, D., Cheng, B., Yu, J.: Adsorption investigation of CO<sub>2</sub> on g-  
776 C<sub>3</sub>N<sub>4</sub> surface by DFT calculation. *J. CO<sub>2</sub> Util.* 21, 327–335 (2017).  
777 <https://doi.org/10.1016/j.jcou.2017.07.021>
- 778 51. Gholivand, K., Alavinasab Ardebili, S.A., Mohammadpour, M., Eshaghi Malekshah,  
779 R., Hasannia, S., Onagh, B.: Preparation and examination of a scaffold based on  
780 hydroxylated polyphosphazene for tissue engineering: In vitro and in vivo studies. *J.*  
781 *Appl. Polym. Sci.* 139, 52179 (2022). <https://doi.org/10.1002/app.52179>
- 782 52. Zaboli, A., Raissi, H., Farzad, F., Hashemzadeh, H.: Assessment of adsorption  
783 behavior of 5-fluorouracil and pyrazinamide on carbon nitride and folic acid-  
784 conjugated carbon nitride nanosheets for targeting drug delivery. *J. Mol. Liq.* 301,  
785 112435 (2020). <https://doi.org/10.1016/j.molliq.2019.112435>
- 786 53. Zhang, H., Ma, L., Ming, J., Liu, B., Zhao, Y., Hou, Y., Ding, Z., Xu, C., Zhang, Z.,  
787 Long, J.: SC State Key Lab of Photocatalysis on Energy and Environment , College of



788 Chemistry ,. "Applied Catal. B, Environ. (2018).

789 <https://doi.org/10.1016/j.apcatb.2018.10.024>

790